minerals

*Type of the Paper (Article, Review, Communication, etc.)*

# Archaean gold mineralization in an extensional setting: the structural history of the Kukuluma and Matandani deposits, Geita Greenstone Belt, Tanzania

**Shimba D. Kwelwa[1,3], Paulus H.G.M. Dirks[1,2] , Ioan V. Sanislav[1,2,*], Thomas Blenkinsop[4] and Sergio L. Kolling[3]**

[1] Economic Geology Research Centre (EGRU), Townsville, 4811, QLD, Australia; s.kwelwa@anglogoldashanti.com
[2] Department of Geosciences, James Cook University, Townsville, 4811, QLD, Australia; paul.dirks@jcu.edu.au
[3] Geita Gold Mine, Geita, P.O. Box 532, Geita Region, Tanzania; skolling@anglogoldashanti.com
[4] School of Earth & Ocean Sciences, Cardiff University, Cardiff CF10 3AT, United Kingdom; blenkinsopT@cardiff.ac.uk
* Correspondence: ioan.sanislav@jcu.edu.au; Tel.: +61-07-4781-3293

Academic Editor: name
Received: date; Accepted: date; Published: date

**Abstract:** Three major gold deposits, Matandani, Kukuluma and Area 3, host several Moz of gold, along a ~5 km long, WNW trend in the E part of the Geita Greenstone Belt, NW Tanzania. The deposits are hosted in Archaean volcanoclastic sediment and intrusive diorite. The geological evolution of the deposits involved three separate stages: (1) an early stage of syn-sedimentary extensional deformation ($D_1$) around 2715 Ma; (2) a second stage involving overprinting ductile folding ($D_{2-4}$) and shearing ($D_{5-6}$) events during N-S compression between 2700-2665 Ma, coeval with the emplacement of the Kukuluma Intrusive Complex; and (3) a final stage of extensional deformation ($D_7$) accommodated by minor, broadly E-trending normal faults, preceded by the intrusion of felsic porphyritic dykes at ~2650 Ma.

The geometry of the ore bodies at Kukuluma and Matandani is controlled by the distribution of magnetite-rich meta-ironstone, near the margins of monzonite-diorite bodies of the Kukuluma Intrusive Complex. The lithological contacts acted as redox boundaries, where high-grade mineralization was enhanced in damage zones with higher permeability including syn-$D_3$ hydrothermal breccia, $D_2$-$D_3$ fold hinges and $D_6$ shears. The actual mineralizing event was syn-$D_7$, and occurred in an extensional setting that facilitated the infiltration of mineralizing fluids. Thus, whilst gold mineralization is late-tectonic, ore zone geometries are linked to older structures and lithological boundaries that formed before gold was introduced.

The deformation-intrusive history of the Kukuluma and Matandani deposits is near identical to the geological history of the world-class Nyankanga and Geita Hill deposits in the central part of the Geita Greenstone belt. This similarity suggests that the geological history of much of the greenstone belt is similar. All major gold deposits in the Geita greenstone belt lack close proximity to crustal-scale shear zones, are associated with intrusive complexes and volcanics that formed in an oceanic plateau rather than subduction setting, and formed late-tectonically during an extensional phase. They are not characteristic of typical orogenic gold deposits.

**Keywords:** Archaean gold; Tanzania; structural controls; deformation; Kukuluma; Geita; orogenic gold.

---

## 1. Introduction

Archean deposits are a major source for gold across most cratonic regions in the world [1-4]. Except for gold deposits linked to supra-crustal basins such as the giant deposits in the Witwatersrand Basin, the bulk of Archean gold is hosted within, or adjacent to greenstone belts, and they are commonly classified as orogenic gold deposits [5-7] [8,9], or Archaean lode gold deposits, to use a less generic term.

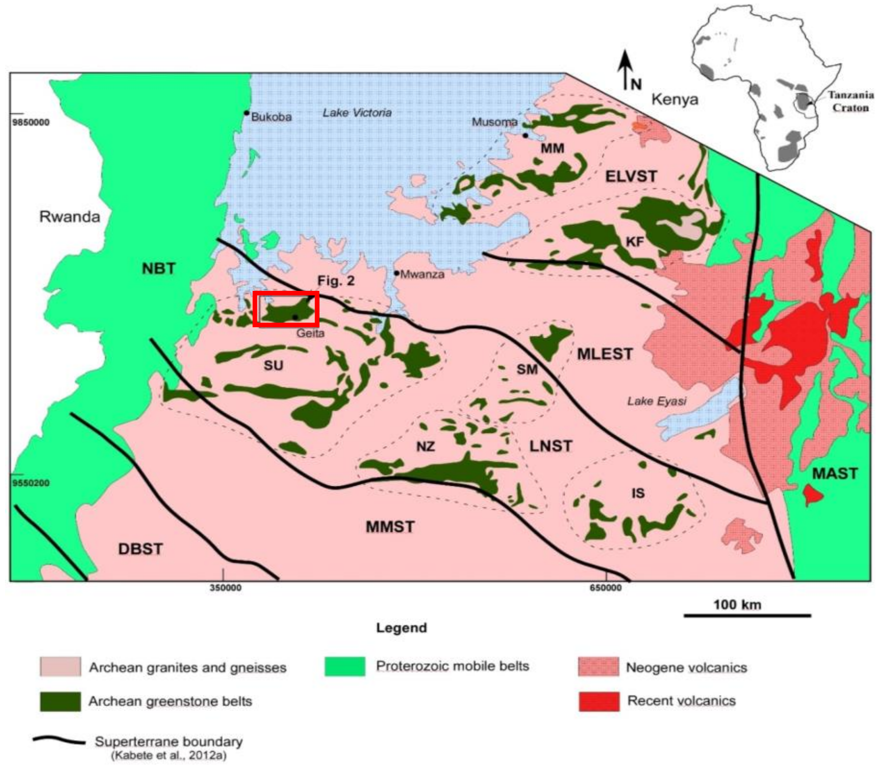


**Figure 1.** Geological map of the northern half of the Tanzania Craton showing the main geological and tectonic units. IS—Iramba-Sekenke Greenstone Belt; KF—Kilimafedha Greenstone Belt; MM—Musoma-Mara Greenstone Belt; NZ — Nzega Greenstone Belt; SM—Shinyanga-Malita Greenstone Belt; SU — Sukumaland Greenstone Belt. Super-terrane boundaries are as proposed by [10]: DBST — Dodoma Basement; ELVST— East Lake Victoria; LNST — Lake Nyanza; MAST — Mbulu-Masai; MLEST —Mwanza Lake Eyasi; MMST —Moyowosi-Manyoni; NBT — Nyakahura-Burigi. The inset map of Africa shows the location of Archaean blocks. The figure has been adapted from [11]. The red square shows the study area as shown in Figure 2.

Archean orogenic gold deposits show many common features including a common association with major fault systems that cut volcano-sedimentary sequences in greenstone belts (e.g. [12] [4]). These faults channel mineralising fluids from deeper crustal levels to traps in an episodic manner through seismic pumping [13,14]. The fluids that transport the gold are typically aqueous-carbonic fluids, with 5–20 mol% $CO_2$, derived from metamorphic devolatilization reactions [8] , and are associated with quartz-carbonate alteration and a low-sulphidation ore assemblage dominated by pyrite-arsenopyrite, with deposition typically (but not exclusively) occurring in greenschist facies domains [15] [6].

Whilst many studies of world-class gold deposits in well-endowed areas such as the Yilgarn and Superior cratons suggest that mineralization involved multiple stages of gold enrichment [15,16] [17-19], evidence for this can be equivocal, because of the complexities associated with structural overprints and reactivations of peak-metamorphic shear zones during later events [20]. Some authors [9] argue strongly that the notion of multiple mineralizing events is wrong, and that all orogenic gold deposits, including the Archean deposits, form during a single late-tectonic stage in a subduction-related tectonic setting in accretionary to collisional orogenic belts, where fluid flow is driven by a change in far-field stress shortly before cratonization [9]. By classifying the deposits in this way Archaean gold deposits are placed in a plate-tectonic setting that is similar to today; a contention that remains strongly contested [20-24].

Because gold mineralization occurs late in most granite-greenstone terrains [2,6,9,20] irrespective of what underlying tectonic model is applied, gold trapping structures can be highly diverse in geometry, and will be controlled by the interplay of multiple overprinting deformational and intrusive events [9]. To understand the detailed structural architecture of a greenstone sequence in relation to the timing of mineralization is, therefore, important when working out gold distribution patterns. The aim of this study is to do this, for a set of major gold deposits in a relatively poorly known greenstone sequence in the Lake Victoria goldfield in Tanzania (Figs 1, 2)

The Geita Greenstone Belt (GGB) in the N part of the Tanzania Craton (Fig. 1) hosts world-class gold deposits spread along a 35 km long corridor in the central parts of the greenstone belt (Fig. 2). These deposits, include (from W to E) the Star and Comet, Nyangkanga, Lone Cone, Geita Hill, Matandani and Kukuluma deposits (Fig. 2), and are commonly referred to collectively as Geita mine [7]. All these deposits are largely hosted in silicified, magnetite-rich metasedimentary units (referred to in the mine as meta-ironstones) near the intrusive contacts of monzonitic to dioritic bodies that intruded internal to the greenstone belt [11,25-27].

To date no detailed work has been published for the major deposits that occur in the eastern part of the GGB (Figs. 2, 3). These include the Matandani, Kukuluma and Area 3 deposits that collectively host several Moz of gold. In this paper, a deformation model for the area around the Matandani and Kukuluma pits will be presented, based on detailed mapping and core logs from the pits and surrounding areas. The deformation model will be linked to the relative timing of intrusive units and gold mineralization, and forms the basis for geochemical and geochronological studies in the area [27,28].

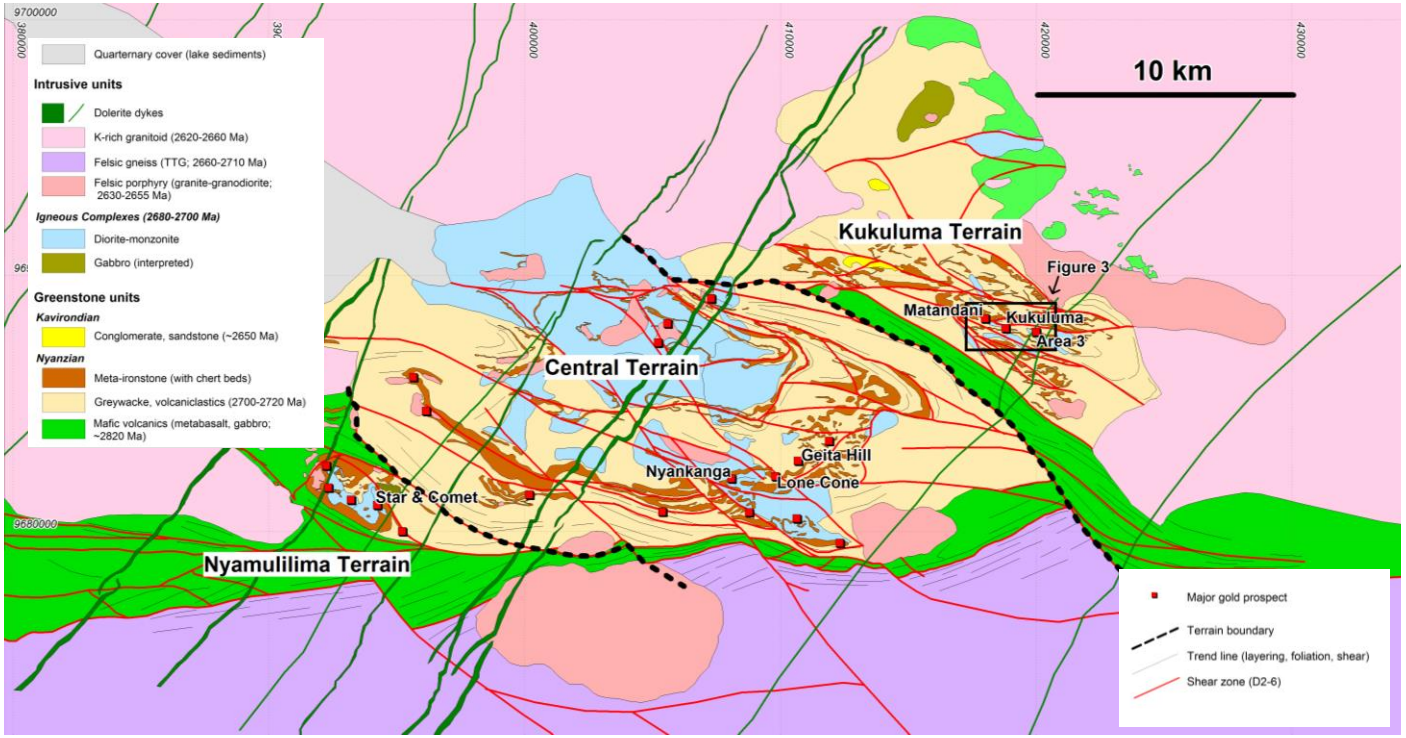


**Figure 2.** Geological map of the Geita Greenstone belt showing the location of the major gold deposits and the main geological terrains, lithological units and structures (listed ages from [11] [28,29]. The Insert shows the study area in figure 3. The grid is in UTM WGS84, zone 36S.

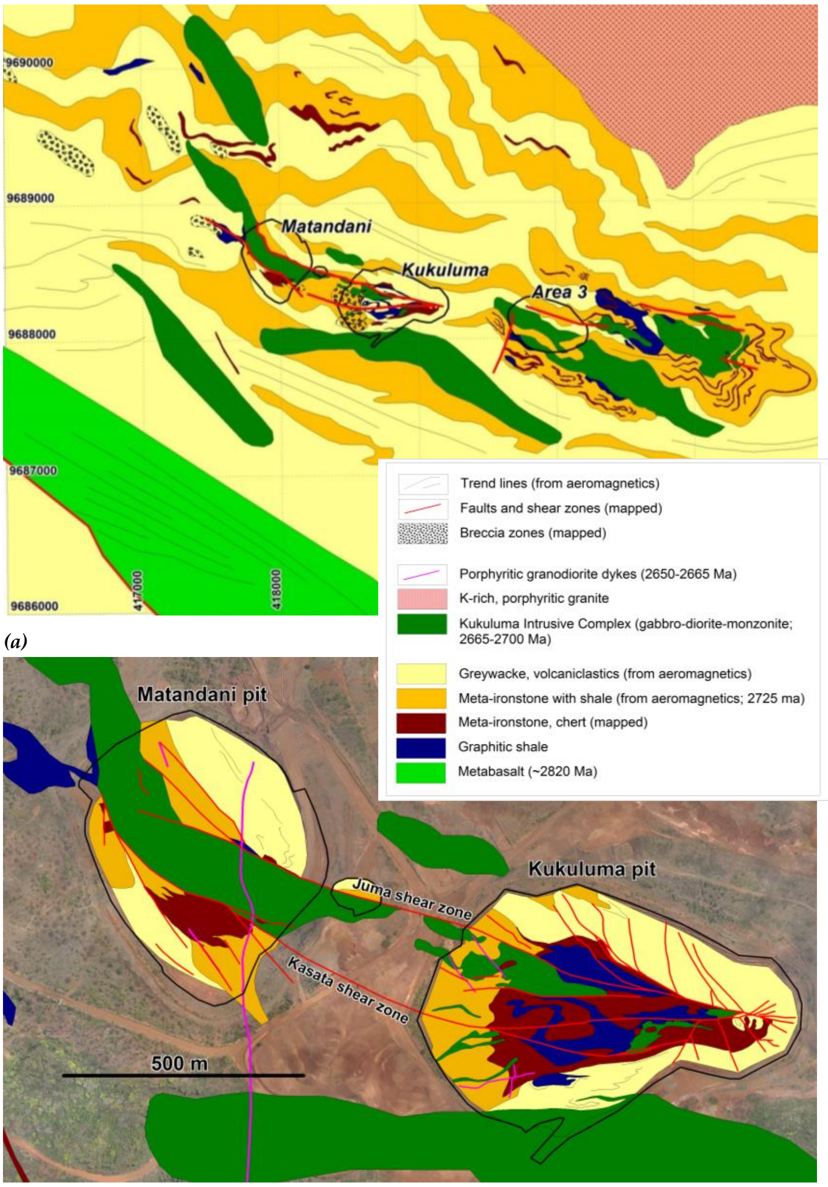


***(a)***

***(b)***

**Figure 3.** (a) Geological map of the central Kukuluma Terrain showing the position of the main gold deposits in the area. The distribution of the meta-ironstones in the area is derived from geophysics. Map projection is UTM WGS84 zone 36S. (b) close-up view of the Matandani and Kukuluma pits. The age estimates in the legend are from [28-30].

## 2. Regional geological framework

The Tanzania craton consists of a core of >3.0 Ga, high-grade mafic and felsic granulite (the Dodoman Supergroup), overlain by a volcano-sedimentary package dominated by mafic volcanics (the 2820-2700 Ma Nyanzian Supergroup), and younger (<2650 Ma), mostly coarse clastic sediment of the Kavirondian Supergroup [31-37]. Rocks belonging to the Dodoman Supergroup are restricted to the southern part of the craton, with the northern craton comprised of younger (<2.82 Ga), juvenile crust [36,38,39]. The latter has been alternatively interpreted as accretionary volcanic arc systems [40] or vertically accreting and chemically evolving oceanic plateaus [39] that docked with the older cratonic core during the Neoarchaean.

The Nyanzian and Kavirondian sequences in the northern part of the Tanzania Craton have been grouped into six greenstone belts (Fig. 1) clustered around the margins of Lake Victoria [34]. Each of these greenstone belts comprises a series of disconnected greenstone domains that were grouped based on perceived stratigraphic correlations and geographic proximity [41], in spite of the presence of large shear zones that separate parts of each greenstone belt [10]. Of the six greenstone belts, the Sukumaland Greenstone Belt is the largest, containing fragments that are large enough, and tectonically and stratigraphically distinct enough to be categorized as greenstone belts in their own right. This includes a greenstone domain along the northern margin of the Sukumaland Greenstone Belt, which we have termed the Geita Greenstone Belt (Fig. 2), following terminology introduced by [11,37].

### *2.1. The Geita Greenstone Belt (GGB)*

The Geita Greenstone Belt (GGB, Fig.2) forms an 80 x 25km large, generally E-W trending portion of mafic- felsic volcanic, volcanoclastic and sedimentary rocks, bounded to the S by a large, E-W trending shear zone that separates the belt from gneiss and mylonitic granitoid [29]. To the N, E and W the greenstone units were intruded by late syn- to post-tectonic granitoid plutons dated at 2660-2620 Ma [30]. The S part of the GGB contains meta-basalt with minor gabbro and a MORB-like affinity, yielding ages of ~ 2823 Ma [36,37], which were deposited through vertical melt segregation in an oceanic plateau environment [37,39]. The remainder of the greenstone belt is dominated by meta-ironstone units intercalated with, and overlain by turbiditic meta-sedimentary units and volcanoclastic beds older than 2699 ± 9 Ma [11,35]. These units were intruded by syn-tectonic igneous complexes of dioritic to tonalitic composition [11,26,27]. The diorite intrusive complex around Nyankanga and Geita Hill were dated at 2686 ± 13 Ma and 2699 ± 9 Ma (U-Pb zircon, [35]), and the intrusive complex around Kukuluma at between 2717 ± 12 Ma and 2667 ± 17 Ma (Figs 2, 3, [27,28]).

Meta-ironstone units are exposed in three distinct NW-SE trending terrains separated by areas with little or no outcrop underlain by meta-sediments. The boundaries of these terrains are characterized by major lineaments visible on aero-magnetic datasets and interpreted as large shear zones (Fig. 2). These terrains are the Nyamulilima terrain to the W, the Central terrain in the middle, and Kukuluma terrain to the E (Fig. 2). The Kukuluma terrain contains the Matandani and Kukuluma deposits, which were mined until 2007 (Figs 2, 3). The nearby Area 3 deposit is undeveloped.

Initial models for the deformation history of the GGB invoked early upright folding, overprinted by a second folding event characterized by steeply plunging axes and cut by later regional and subsidiary shear zones, which represent the main pathways for hydrothermal fluids [25,33,41]. Mine models in the early 2000's assumed that mineralized shear zones in the GGB were part of complex thrust stacks associated with horizontal shortening and stacking of the greenstone sequence with gold-mineralization concentrating in dilatant zones along thrusts and near fold hinges [42,43]. Subsequent mining has demonstrated that complex thrust stacks with stratigraphic duplication do not exist, but instead that gold is related to a complex interplay of folding and intrusive events cut by late, mainly E-trending fracture zones as seen in the Nyankanga and Geita Hill deposits (Fig. 2, [11,26]). Detailed structural work in these deposits [11,26] has shown that the mineralization is centered on NW dipping reverse faults (referred to in Geita Hill as $D_6$) that overprint a complexly folded (referred to in Geita Hill as $D_{1-5}$) stack of meta-ironstone and chert, and were reactivated as later normal faults at the time of mineralization (called $D_8$ at Geita Hill). Gold-deposition preferentially occurred along diorite-meta-ironstone contacts exploited by the fracture systems [11,26] after emplacement of a lamprophyre dyke at 2644 ± 3 [35] i.e. Ma 20-30 Ma later than the formation of reverse faults [26].

### *2.2. Stratigraphy of the Kukuluma terrain*

A generalized stratigraphic column for the Kukuluma terrain is presented in Figure 4. This column has been reconstructed from mapping and drilling around the Kukuluma and Matandani pits as presented in this study, combined with age constraints from intercalated volcaniclastics and cross cutting porphyry dykes [28]. The Kukuluma terrain is bounded to the W by a major NW-trending shear zone, which juxtaposes lower greenschist facies meta-sediments of the Central terrain, and lower amphibolite facies mafic to ultramafic meta-basalts at the stratigraphic base of the Kukuluma terrain (Fig. 2; [37]).

The sedimentary sequence in the central parts of the Kukuluma terrain is composed of a volcano-sedimentary pile with a black, graphitic shale unit of undefined thickness (pit outcrops indicate a minimum thickness of ~30 m) at its base. This unit is well exposed at the bottom of the Kukuluma pit, and probably overlies metabasalt [28]. The black shale unit transitions into a well-layered meta-ironstone unit that is variable in thickness due to deformational effects (described below). The meta-ironstone unit is widely distributed (Fig. 3), and consists of regularly layered packages of magnetite-rich sandstone and siltstone interlayered with shale beds and silicified, quartzite beds. The meta-ironstone unit transitions into meta-greywacke comprised of laminated shale- to sandstone beds (Fig. 4) interlayered with fine-grained meta-tuff and volcaniclastics. The greywackes have characteristics similar to deposits laid down on the proximal parts of a marine fan-delta system with input of immature sediment [44]. Rocks of the Upper Nyanzian are intruded by diorites, monzonites and granodiorites of the Kukuluma Intrusive Complex (Fig. 4). In the N part of the Kukuluma terrain, the meta-ironstone and meta-greywacke units are unconformably overlain by cross-bedded sandstone and clast supported conglomerate ascribed to the Kavirondian Supergroup.

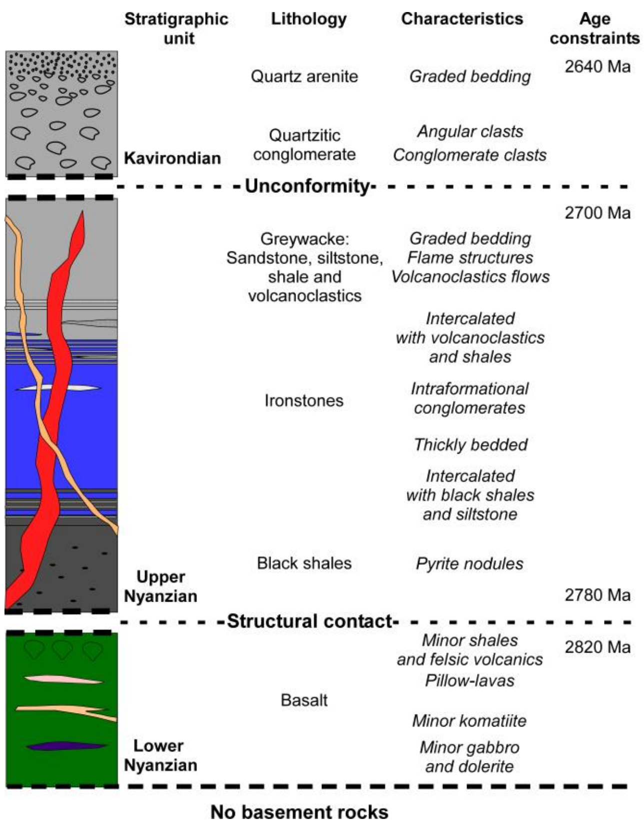


**Figure 4.** Summary stratigraphy for the Kukuluma terrain. Age constraints are from [28,37].

**Table 1.** Summary of deformation and intrusive events that affect the Kukuluma terrain. Listed age estimates are based on [11,28,29]. Mineralization occurs during $D_7$ events, and gold-bearing fluids are trapped in structures of $D_1$ to $D_6$ origin. Apy = arsenopyrite; Po = pyrrhotite; Py = pyrite

| **Deform. event** | **Intrusive event [age]** | **Description of structures** | **Mineralization [Trapping structures]** |
|---|---|---|---|
| *$D_1$* | Volcanism<br>**(2715 Ma)** | - Layer-parallel shears<br>- Growth faulting | (1) Mineralisation trapped by Fe-rich lithologies |
| *$D_2$* | | - Non-cylindrical folding (1-500 m scale)<br>- Formation of penetrative $S_2$ fabric | (2) Mineralization in $F_2$-$F_3$ fold hinge zones |
| | Start of emplacement of KIC:<br>Gabbro-diorite-monzonite suite<br>**(2700-2680Ma)** | - Sills, dykes and plugs | (3) Mineralization along diorite-ironstone contacts |
| *$D_3$* | Further emplacement of KIC :<br>Gabbro-diorite-monzonite suite<br>**(2700-2680Ma)** | - Folding on 1-500 m scale<br>- Plunge varies across $F_2$ fold limbs<br>- Associated with $S_3$ axial planar cleavage that dips steeply SW<br>- High-strain domains bound folded domains<br>- Emplacement of KIC along $D_3$ axial planes with $S_3$ fabric in KIC<br>- Extensive brecciation of $D_2$-$D_3$ folded ironstone near margins of KIC | (4) Mineralization trapped along $F_3$ fold axial planes characterized by microfracturing<br><br>(5) Mineralization in breccia zones |
| *$D_4$* | | - Open, cylindrical upright folding<br>- Symmetric folds plunge steeply WNW<br>- Limited $S_4$ fabric development | |
| *$D_5$*<br>N-S compression<br> | Further emplacement of KIC:<br>Granodiorite suite<br>**(2680-2665 Ma)** | - Open cylindrical recumbent folds<br>- low angle reverse faults with small offsets (<10m)<br>- Felsic porphyry dykes truncate $D_{1\text{-}4}$ folds | |
| *$D_6$*<br>N-S compression<br> | | - NW to WNW trending, steeply dipping, brittle ductile shear zones.<br>- Dextral-reverse<br>- Fracture networks overprint $F_2$-$F_3$ folds and breccia zones<br>- Associated with tectonic breccia | (6) $D_6$ shear zones and associated damage zones facilitate fluid infiltration and fluid-rock interaction |
| | Emplacement of felsic dykes **(2650Ma)** | - N trending felsic porphyry dyke | Mineralization overprints dykes |
| *$D_7$*<br>N-S extension<br> | | - Normal faulting<br>- Reactivation of $D_6$ shears as sinistral normal faults | (7) $D_7$ shear zones are mineralized, and acted as the main fluid channel ways<br><br>apy-po-py ore assemblage |
| | Granitoids plutons<br>**(2620-2640 Ma)** | | |

## 3. The history of deformation in the Kukuluma terrain

The deformation events in the Kukuluma-Matandani area comprise 3 groups of structures: 1. structures that formed during an extensional deformation episode ($D_1$) at the time of sedimentation and early volcanism, which are best preserved in drill core; 2. penetrative structures ($D_2$-$D_6$) involving overprinting folding, shearing and brecciation events, which occurred when the rocks mostly behaved in a ductile manner during the main compressional stage of deformation; and 3. localized late tectonic structures that formed during extensional deformation, when strain was partitioned into discrete normal faults and joints ($D_7$). Deformation events were accompanied by the emplacement of syn-tectonic intrusions of the Kukuluma Intrusive Complex (KIC, [27]). A mineralized, late-tectonic felsic porphyry dyke cross-cuts all units, and provides an upper age constraint for gold mineralization in the area [28].

The deformation events have been summarized in Table 1 and are described in detail below. In reading the deformation history it is important to realize that $D_1$-$D_6$ deformation geometries in combination with intrusive boundaries, provide the deformational architecture that trap the auriferous fluids, which percolated late in the deformation history of the area [9].

### *3.1. $D_1$- normal faulting and bedding parallel shearing events*

$D_1$ comprises a complex family of structures that formed prior to the development of $D_2$ folds. These structures formed in part during sedimentation of the meta-ironstone and meta-greywacke sequences, and partly after these units were buried (presumably as extension-sedimentation continued higher up in the stratigraphy). Centimeter-scale growth faulting visible in drill core in meta-sediment indicate active extension during sedimentation. In places the growth faults are listric and associated with layer-parallel zones of brecciation and folding characterized by cm- to dm-scale disharmonic folding interpreted as layer-parallel deformation zones similar to low-angle detachments.

Meta-ironstone units preserve an early-layer-parallel foliation, $S_1$ that locally intensifies. A good example of this occurs along the access ramp into Kukuluma pit between GR 418900-9688150 and 418950-9688180 (all grid references in WGS84, zone 36S), where a well-layered greywacke unit is intruded by dark-grey, planar quartz veins with a chert-like appearance (Fig. 5a). Over a horizontal distance of about 15 m the density of these intrusive veins increases as the rock changes from bedded meta-greywacke into a massive glassy chert, and coarser grained sandstone beds are boudinaged. $S_1$ is well-developed in this zone together with rare intrafolial folds, dextral shear bands and an $L_1$ mineral lineation, and the zone is interpreted as a $D_1$ shear zone. Although the shear sense across this zone is unclear, it cuts out part of the stratigraphy, which together with the associated boudinaging and extension of the host rock layering suggests an extensional origin. It may link to basin opening and is interpreted to represent a deeper level manifestation of the syn-sedimentary growth faults seen in drill core.

Similar discordant chert horizons displaying complex internal folding and fine-grained fabrics with mylonitic affinities are common throughout the central Kukuluma terrain. In many places (e.g. Fig. 5b) the chert layers transect bedding in the surrounding meta-ironstone or meta-greywacke units at a low angle. In other places the orientation of chert beds is parallel to layering within the wall rock (Fig. 5c). On a regional scale, the chert bands form low ridge lines that can be traced for several kilometers (Fig. 3). The chert horizons display sudden thickness variations along strike, and in places bifurcate or merge to form anastomosing patterns. The chert bands are affected by all later folding events described below, and formed early in the tectonic history of the Kukuluma terrain.

### *3.2. $D_2$-$D_3$ folding and shearing*

The composite $S_1/S_0$ fabric in the central Kukuluma terrain was folded and sheared during $D_2$ and $D_3$ events (Figs 6, 7, 8). This has resulted in locally complex, $D_2$-$D_3$ interference folding of the volcano-sedimentary stratigraphy, including those units that preferentially host gold mineralization.

$F_2$ folds occur on outcrop scale as tight to isoclinal folds that develop a penetrative axial planar cleavage in fine-grained shale. $F_2$ fold axes are highly variable in orientation (Fig. 6~~b~~), in part due to the non-cylindrical nature of $D_2$ folds [26], and in part due to later folding overprints causing regional (domainal) variability in the $D_2$ fold axes. In single outcrops where $F_2$-$F_3$ interference folding is well developed (e.g. Fig. 8), the orientation of $F_2$ fold axes varies from near-parallelism with $F_3$ fold axes, to high angles to $F_3$ fold axes; a trend reflected in stereoplots of $F_2$ (Fig. 6). The existence of large-scale (>100 m) $D_2$ folds is evident from the regional distribution patterns of chert ridges (Fig. 3), and can also be inferred from the domainal distribution of $D_3$ fold axes orientations (Fig. 6) as explained below.

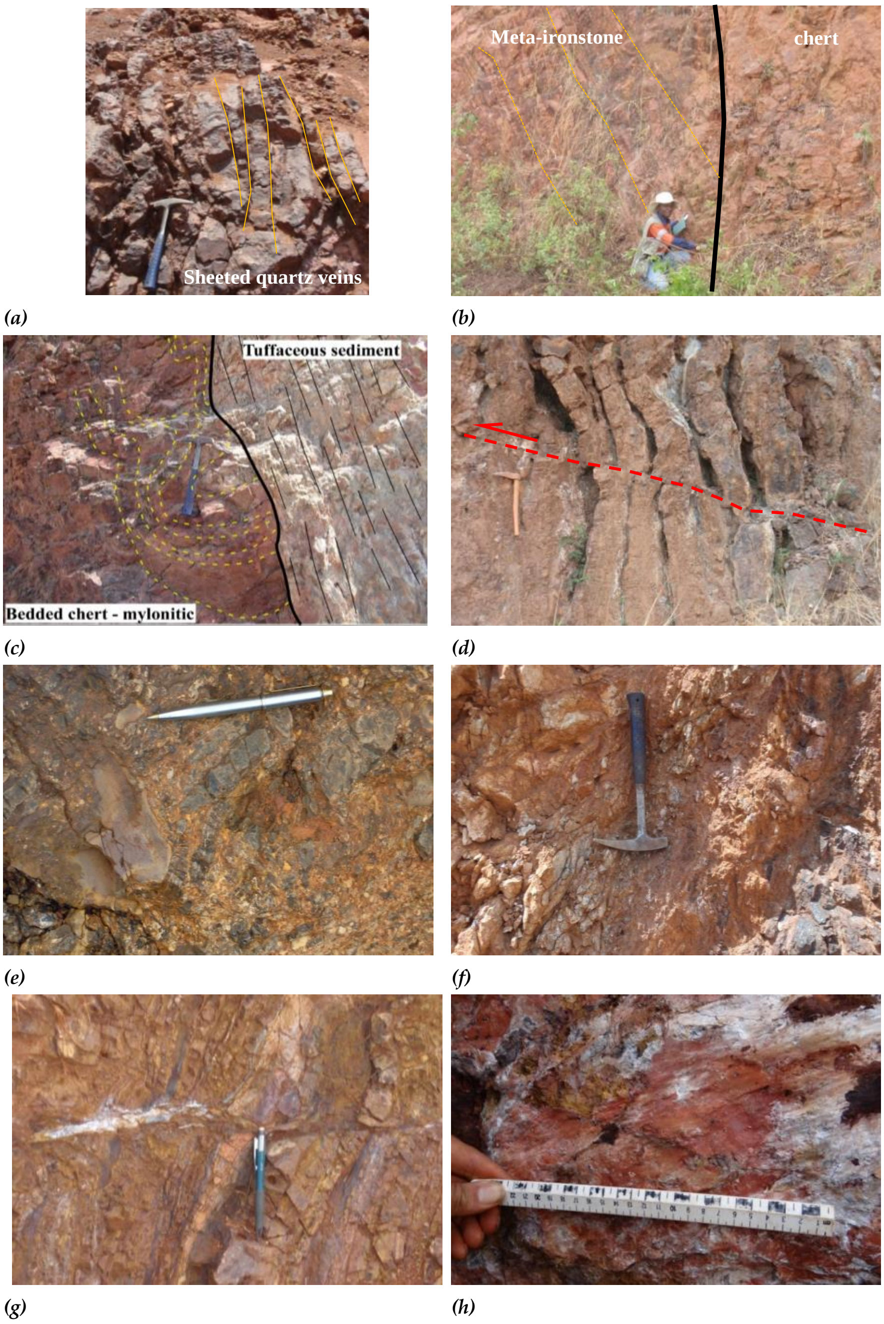
Sheeted quartz veins
(a)
Meta-ironstone
chert
(b)
Tuffaceous sediment
Bedded chert - mylonitic
(c)
(d)
(e)
(f)
(g)
(h)

**Figure 5.** Examples of shear zones in the Kukuluma terrain: (a) Closely spaced magnetite-bearing sheeted quartz veins intruded along a $D_1$ shear zone (Kukuluma pit); (b) Planar chert ridge (right) cuts at a low-angle through primary bedding in a meta-ironstone unit along access road to Kukuluma. The chert is interpreted as a $D_1$ shear zone; (c) Planar chert horizon E of Area 3. The margin of the chert parallels $S_0$ in the surrounding sediments, but internally the chert is folded with mylonitic characteristics attributed to $D_1$; (d) $D_5$ low-angle reverse fault and associated recumbent folding in chert in Kukuluma pit; (e) Cataclasite and tectonic breccia zone along $D_6$ shear zone in chert in Kukuluma pit; (f) $D_6$, Kasata shear in NW corner of Matandani pit; (g) $D_7$ fracture plane characterized by the presence of (white) sericite and sulphide alteration in artisanal workings along W wall of Matandani pit; (h) $D_7$ fracture plane with (white) sericite and slickenlines indicative of normal-sinistral movement in artisanal workings along W wall of Matandani pit**.**

$D_3$ folds are common and comprise upright to vertical folds that vary from open to near-isoclinal, with tightening of the folds occurring near planar high strain zones. The $S_3$ axial planar surface is generally near vertical and varies in trend from W to NW with orientations in the pits showing two clear maxima around 210/80 and 350/75 (Fig. 6c) as a result of $D_4$ folding (discussed below). $S_3$ fabrics vary in character from well-developed, closely spaced (<1 mm) planar crenulation cleavages in shale (Fig. 7c), to more widely spaced, fracture cleavages in more competent silicified meta-ironstone beds.

The orientation of $F_3$ fold axes varies in a systematic manner across the pits as a result of $D_2$-$D_3$ fold interference (Fig. 6). Along the S wall and W ramp of Kukuluma pit, $F_3$ fold axes generally plunge shallowly E (ave. $F_3$ = 091/17; Fig. 6c). Towards the N wall of Kukuluma pit, $F_3$ fold axes rotate to near-vertical (ave. $F_3$ = 287/83; Fig. 6c). The same near-vertical $D_3$ fold orientation also dominates outcrops in the area between Kukuluma and Matandani pits, and in the SW wall of Matandani pit. Towards the NE wall of Matandani pit, $F_3$ fold axes vary between a near vertical plunge and a gentle NW-SE plunge Fig. 6c). The bimodal distribution of $F_3$ fold axes indicates that large-scale $D_2$ folds are present, with the hinge zone of one such fold trending in a general NE direction along the NW margin of Kukuluma pit, and a possible second $F_2$ hinge zone passing through Matandani pit. Before upright $D_3$ folding, the orientation of the composite $S_0$/$S_1$ layering would have varied from steeply N to NW dipping in the S-part of Matandani pit and the area between Matandani and Kukuluma pits, to generally shallow dipping layering in most of Kukuluma pit and the N part of Matandani pit. This pattern suggests the presence of a 500 m scale, possibly SE verging, asymmetric antiformal $D_2$ fold with a NW dipping axial planar surface.

Outcrop scale vergence of $D_3$ folds varies across the pits, reflecting large-scale $D_3$ folding. Along the S and W walls of Kukuluma pit, $D_3$ folds generally verge N, whereas $D_3$ folds along the N wall of the pit verge S. This suggests that Kukuluma pit is positioned in the centre of a 500 m scale E to SE trending, upright $D_3$ fold and occurs together with Matandani pit along the hinge zone of a large-scale $D_3$ anticlinorium.

$D_2$-$D_3$ fold interference patterns are common on outcrop-scale (e.g. 0418140-9688080; Fig. 8) and are generally of type 2 [45,46]. Interference patterns are characterized by crescent and hook shapes (Fig. 8) and locally converge to type 3 fold patterns where $F_2$ and $F_3$ fold hinges reach near-parallelism [45]. Around Area 3, chert ridges define 500-800 m scale type 2 fold interference patterns (Fig. 3).

**Formatted:** Subscript

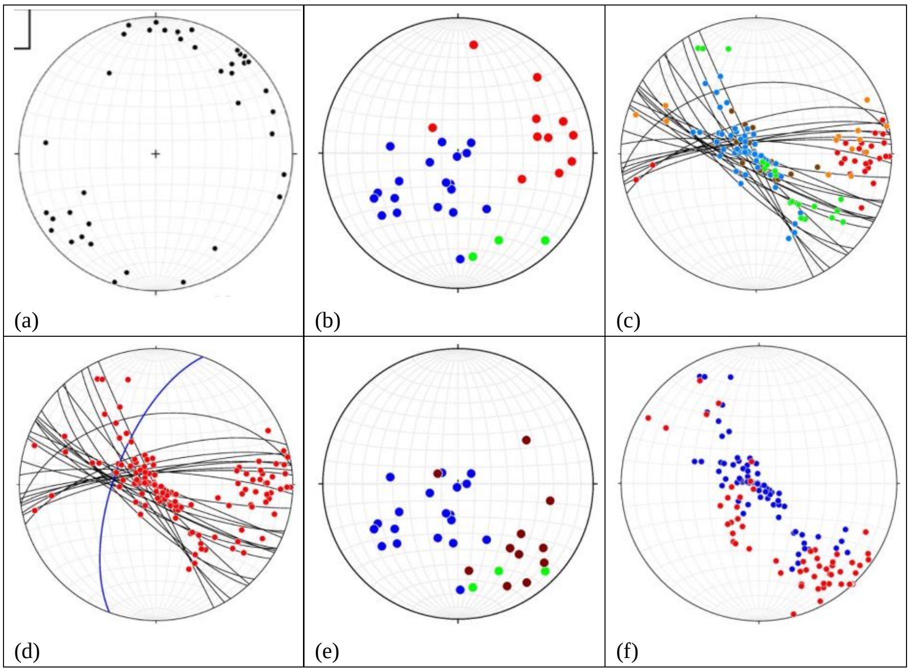


**Figure 6.** (a) Orientation of poles to the intrusive diorite-sediment contacts as observed in drill core and the field (N=38); (b) Orientation of $F_2$ fold axes in Kukuluma and Matandani pits (N = 33). Colour coding: red = S ramp in Kukuluma pit; blue = SW side in Matandani pit; green = NE side in Matandani pit; (c) Orientation of $S_3$, fold axial planes (great circles) and $F_3$ fold axes in Kukuluma and Matandani pits. Colour coding: red = S ramp in Kukuluma pit; orange = W ramp in Kukuluma pit; brown = NW wall in Kukuluma pit; blue = SW side in Matandani pit; green = NE side in Matandani pit; (d) Orientation of $S_3$, fold axial planes (great circles) and $F_3$ fold axes (red dots) in Kukuluma and Matandani pits. $S_3$ and $F_3$ are distributed in two clusters in either limb of $D_4$ folds. $S_4$ (blue great circle) equals the plane bisecting the obtuse angle = 290/65; (e) Orientation of $F_2$ fold axes in Kukuluma and Matandani pits in which the Kukuluma axes have been rotated clockwise by 50 degrees around an axes of 287/65, to remove the effects of $D_4$ open folding. Colour coding: brown = rotated orientations along S ramp in Kukuluma pit; blue = SW side in Matandani pit; green = NE side in Matandani pit; (f) Orientation of $F_3$ fold axes in Kukuluma and Matandani pits in which the Kukuluma axes have been rotated clockwise by 50 degrees around an axes of 287/65, to remove the effects of $D_4$ open folding. Colour coding: red = rotated $F_3$ orientations in Kukuluma pit; blue = $F_3$ orientations in Matandani pit.

Locally $D_2$-$D_3$ fold domains are truncated by planar foliation domains that are unaffected by $D_2$-$D_3$ folding, except for the presence of isoclinal intrafolial folds within the foliation, good examples can be seen along the SE-wall of Matandani pit (e.g. 418180-9688300). These foliation domains trend NW across the central Kukuluma terrain and are generally near-vertical. They contain a moderately to steeply W to NW plunging mineral lineation, $L_3$, that parallels the axes of intrafolial folds within the high strain domains. The layering in these foliation domains is composite in nature with $S_0/S_1/S_2/S_3$

all transposed and parallel to each other, and they developed at the same time as $D_3$ folding. The regional distribution of these $D_3$, high-strain zones cannot be assessed due to poor outcrop exposure.

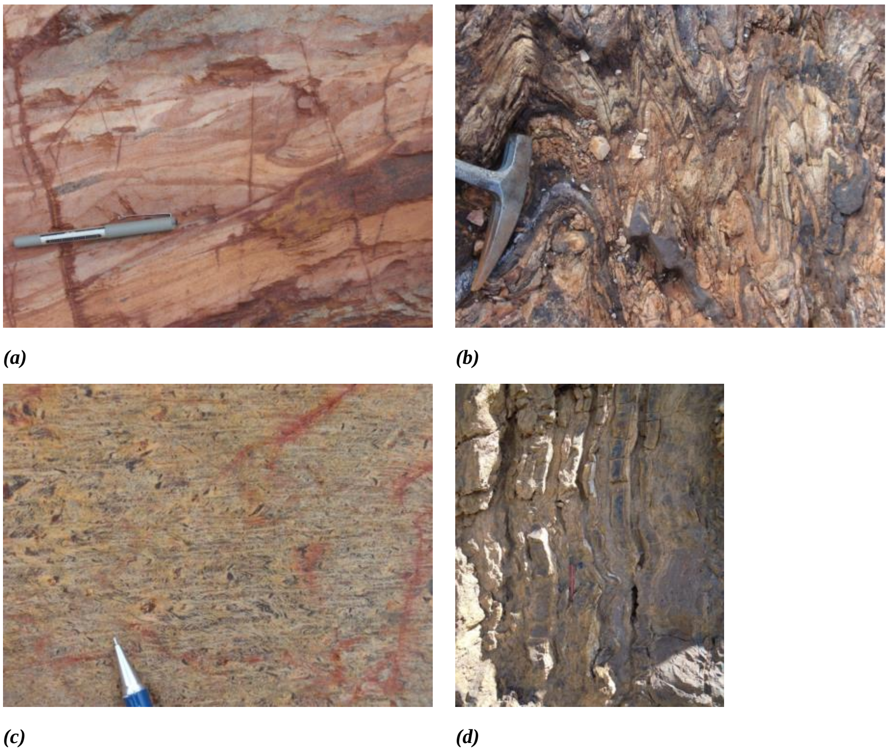


**Figure 7**. Examples of fold structures in the central Kukuluma terrain: (a) ductile, flame-like isoclinal folds in turbiditic greywacke interpreted as folding associated with fluidization during $D_1$; (b) tight $D_3$ vertical folds in ironstone in SW Matandani pit; (c) close up of $S_3$ spaced crenulation cleavage in shale; (d) open recumbent $D_5$ folding in chert bands.

### *3.3. $D_4$ gentle upright folding*

$D_4$ folds are gentle, cylindrical, upright folds with steep axial planes that warp $S_3$ (and earlier foliations) on a 0.5-1 km scale. $D_4$ folds are not clearly visible in outcrop, but can be seen when tracing $D_1$ chert horizons or $S_3$ along strike; e.g. across Kulkuluma pit $S_3$ orientations change from steeply SW dipping (ave. 210/80) in the NW corner of the pit to steeply N dipping (ave. 350/75) across the rest of the pit as a result of large-scale, $D_4$ folding with a steeply W plunging fold axes and NW dipping fold axial plane (Fig. 6d). Similar open folding of $D_3$ structures is apparent across the area (Fig. 3), with the fold axial trace of $D_4$ folds trending roughly NNE-SSW. No penetrative $S_4$ fabric has developed, but where $D_4$ folds affect thick chert layers, e.g. around Area 3 a spaced NNE-trending fracturing can be observed in $D_4$ hinge zones.

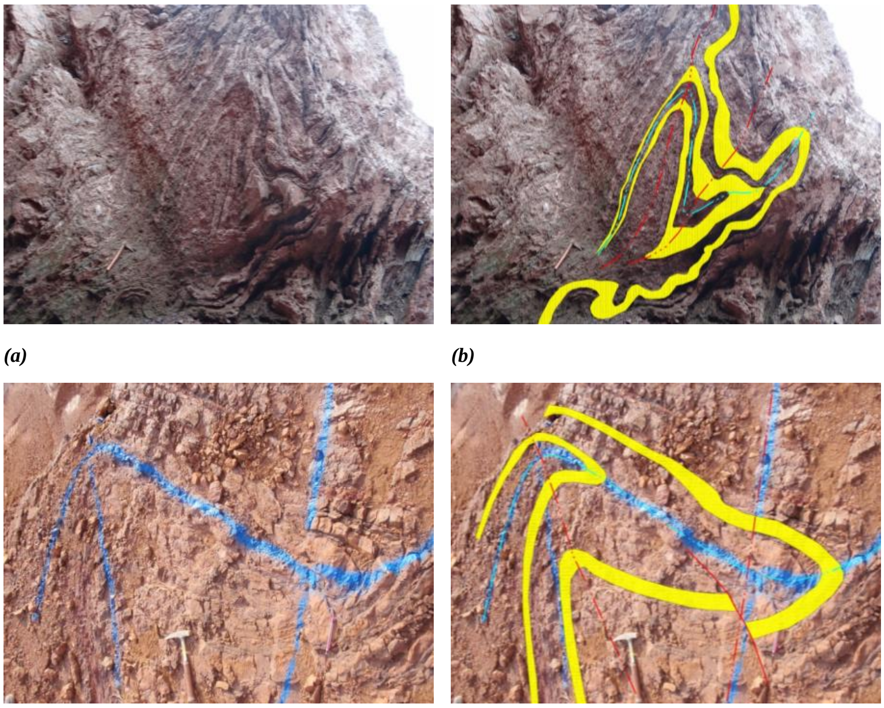

*(a)* *(b)* *(c)* *(d)*

**Figure 8.** Examples of outcrop-scale D2-D3 fold interference patterns in the central Kukuluma terrain shown as annotated pairs. Marker layers have been highlighted in yellow; the $D_2$ fold axial trace is shown in light blue; the $D_3$ fold axial trace is shown in red. (a) & (b) vertical view of fold pair in erosion gully along the E face of Matandani pit; (c) & (d) horizontal view of fold pair on the upper benches in the SW corner of Matandani pit.

### *3.4. $D_5$ recumbent folding and low-angle reverse faulting*

$D_5$ involved localized low-angle reverse faulting and associated recumbent folding that is poorly visible in areas without good vertical exposure. Low-angle reverse fault planes are best developed within the well-bedded ironstone units in the W side of Kukuluma pit (Fig. 5d). Fault zones vary in thickness from several mm to ~20 cm, but are generally thin and discrete, and visible as thin grey clay zones that ramp up through the ironstone units. The larger (i.e. wider) fault zones generally dip gently N (around 000/20), but they locally vary in orientation with secondary fractures moving into parallelism with bedding planes. The faults accommodated reverse movements of up to ~10 m, with most faults accommodating significantly less.

Folding is common in spatial association with the fault planes. $D_5$ folds vary in scale from 0.1-5 m and are generally open recumbent folds with near horizontal to shallowly dipping axial planar surfaces (Figs. 5d, 7d), and shallowly E or W plunging fold axes. In places $D_5$ folds are asymmetric and appear as drag folds associated with the thrusts (Fig. 5d). Elsewhere, $D_5$ folds form open corrugations in well-bedded meta-ironstone, with a widely spaced fracture cleavages.

### *3.5. $D_6$ brittle-ductile shear zones*

A network of generally steeply dipping, NW to WNW trending shear zones can be traced across the central Kukuluma terrain (Fig. 3). These $D_6$ shears crosscut the folded sequence and have been linked to mineralization [47,48]. In the Kukuluma and Matandani pits the system of $D_6$ shear zones is referred to as the Juma and Kasata shear zones (Fig.~~s~~ 3b; [47]. In Area 3 similar W to NW-trending shear zones can be seen in drill core, but poor outcrop prevents these shears from being mapped.

The Juma shear zone can be traced along the entire length of the Kukuluma and Matandani pits, and occurs within the small open pit between Kukuluma and Matandani (Fig. 3b). The shear zone is positioned along the WNW to NW trending N contact of a major intrusive diorite sill belonging to the KIC (~~Figs~~ Fig. 3b; [28]). Towards the E end of Kukuluma pit, the Juma shear terminates into a network of smaller moderately to steeply dipping fracture zones with variable trends (Fig. 3b).

The Kasata shear zone can be traced through the centre of Kukuluma pit as a composite, steeply dipping, and generally W to WNW trending fracture zone. In Matandani pit it re-appears in the S corner of the pit as several WNW trending, semi-parallel fracture zones that merge towards the NW part of the pit into a single NW trending brittle-ductile shear zone that follows the contact of the same intrusive diorite bordering the Juma shear (~~Figs~~ Fig. 3b). In the E part of Kukuluma pit the Juma and Kasata shears merge across a complex network of mostly E-W trending fractures.

Individual $D_6$ shear planes are accompanied by damage zones up to several meters in width that are associated with secondary jointing, brecciation, veining and silicic alteration. Mineralization occurs mainly as disseminated sulphide impregnations along microfractures in the damage zones. Where several shear planes are in close proximity to one another (e.g. in the S corner of Matandani pit, or where the Kasata and Juma shears merge in the E part of Kukuluma pit), up to 15 m wide, extensively fractured and altered (strongly silicificied) domains occur. Where the shears transect micaceous schist, chlorite-muscovite shear bands have developed into S-C like fabrics (e.g. Fig. 5f). Brittle deformation structures (veins, breccia and cataclasite zones) are more common in portions where the shear zone cuts across massive, chert-rich meta-ironstone units (Fig. 9~~e~~). $L_6$ lineations are visible as mineral alignments, striations and quartz rods. In places, mineralization appears to be concentrated along $D_6$ shear zones, but elsewhere (e.g. NW and S walls of Matandani pit; NE corner of Kukuluma pit), well exposed portions of the $D_6$ shears are not mineralized.

The orientations of the $D_6$ fracture zones associated with the Juma and Kasata shears as measured in the Kukuluma pit are shown in Figure 9a. The main strands of the Juma and Kasata shears trend WNW (020/80) with a gently NW or SE plunging lineation recording a dextral sense of movement with a reverse component. A prominent set of, 2nd order shears trends more NW with a steep SW dip (ave. 235/75) and a moderately S plunging lineation recording reverse dextral movements. A third set of, steeply NNW to NW dipping shear zones (ave. 324/72) with moderately to steeply N plunging lineations record sinistral-reverse movements and a fourth set of steeply S dipping, E-W trending faults (ave. 175/76) hosts down dip lineations and a pure reverse (S over N) sense of movement (Fig. 9a). This network of shears is generally non-mineralized, and is consistent with Y-shears (the Juma shear), Riedel shears (NW trending set) and anti-Riedel shears (SW trending set) within a wider dextral transpressional shear system [46], that combines with high-angle reverse faults (the E-trending set). On a larger scale, the distribution of the main $D_6$ shear zones is reminiscent of a right stepping en-echelon array of WNW to NW trending shears within a more E-W trending shear envelope accommodating reverse dextral movement (Fig. 3).

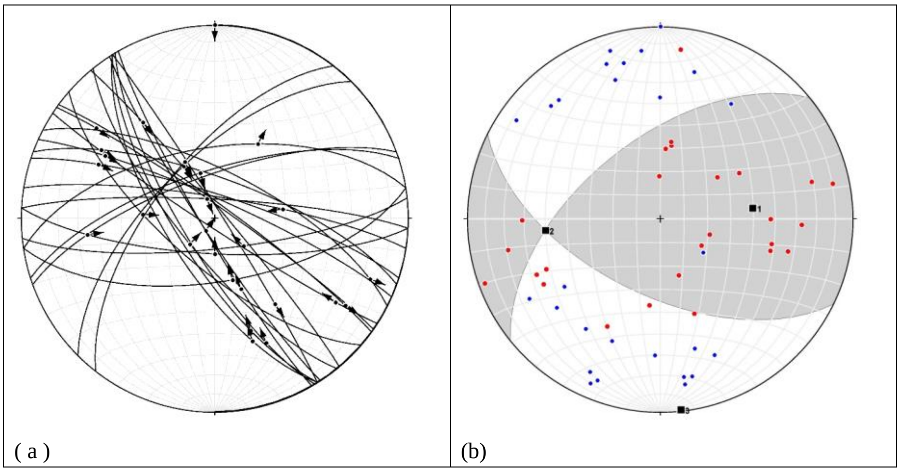


**Figure 9.** Orientation and paleo-stress analysis for $D_6$ shear zones measured in Kukuluma and Matandani pits (N = 27). (a) plot of fault planes and lineations with arrows pointing in direction of movement of the hanging wall; (b) fault plane solution (Bingham matrix solution) for the measured $D_6$ faults (compression dihedron in white; tension dihedron in grey). P axes are shown in blue, T axes in red. The Bingham solution shows N-S shortening with a near-horizontal $\sigma_1$, and a dispersed distribution of P and T axes, i.e. $\sigma_2$ and $\sigma_3$ are similar. Bingham solution:

| Axis | Eigenvalue | Trend | Plunge |
|---|---|---|---|
| 1. ($\sigma_3$) | 0.1918 | 083.1 | 50.2 |
| 2. ($\sigma_2$) | 0.0419 | 264.5 | 39.8 |
| 3. ($\sigma_1$) | 0.2337 | 173.9 | 00.7 |

A paleo-stress analysis for the $D_6$ faults in Kululuma and Matandani pits using Faultkin [20,49,50] was performed on 27 shear planes for which kinematic data was obtained. These shear zones are part of the interconnected network of fractures that form the Juma and Kasata shear network (Fig. 3), and hence it is assumed that they formed simultaneously in response to the same far field stress [20]. In doing the analysis all shear planes were given the same weight; the methodology to conduct paleo-stress analysis has been explained in appendix 1. Results are shown in Fig. 9b, and indicate that the $D_6$ shear zones in the central Kukuluma terrain formed in response to horizontal, near N-S shortening in a plane strain to flattening strain environment (Rev = 0.35)

### *3.6. $D_7$ faulting*

Where $D_6$ shear zones are outcropping they commonly show evidence of reactivation along discrete, mm-wide, $D_7$ fracture surfaces that are slickensided, with slickenfibres defined by sericite and/or quartz (Figs 5g, h). Reactivation of $D_6$ shear zones during $D_7$ is most clearly demonstrated in Matandani pit, where a N-trending porphyry dyke dated at 2651 ± 14 Ma [28] transects the $D_6$ shear fabric, but is fractured and displaced by several centimeters as a result of brittle reactivation along $D_7$ fractures, that form as discrete planes in the center of the $D_6$ shear zone. Where the $D_7$ fractures cut the dyke, an alteration halo of quartz-sericite-sulphide has developed, and the dyke is mineralized. The $D_7$ fracture planes contained as reactivation surfaces in $D_6$ shear zones are generally associated with lineation directions that record a normal sense of movement. A network of well-developed, $D_7$ fracture planes can be seen in the E corner of Kukuluma pit, where they occur near the termination of the Juma shear, and where they are high-lighted by artisanal miners who have excavated high-grade mineralization along the fracture planes.

Away from $D_6$ shear zones, narrow fracture zones attributed to $D_7$ occur in parts of the pits and in Area 3 (Figs 5g, h). Such fractures are mineralized with disseminated sulphide (mainly pyrite) alteration of the wall rocks, and they have the appearance of (shear) joints. The fractures are locally paralleled by thin grey quartz stringers, which return free gold in pan.

In the W wall of Matandani pit, three 15-20 m wide, $D_7$ fracture zones occur to the W of the Kasata shear zone, within deeply weathered layered turbiditic meta-sediment and ironstone. Each fracture zone comprises an interconnected network of variably orientated fractures within envelopes that trend roughly 290-110°. The three fracture zones are arranged in an en echelon array along a NW trend. Within each fracture zone, individual fractures have maximum strike lengths of several 10's of meters, but most are shorter in length. The fractures are narrow (<3 mm) and characterized by sericitic alteration (now mostly visible as white clay staining) with disseminated sulphide (cubic pyrite, now mostly oxidized).

The fault planes preserve excellent slickenlines and shear sense indicators indicative of predominantly sinistral-normal movement (Fig. 5h). Displacements on the $D_7$ fracture planes are small, i.e. in the order of centimeters. To the SE, along the floor of Matandani pit, where the ESE-trending envelope of the fracture planes transects the Kasata shear along the contact of ironstone and diorite, the main ore zone occurs that is targeted by Geita mine (Fig. 3).

Paleo-stress analyses for the $D_7$ fracture zones in Kululuma and Matandani pits using Faultkin [20,49,50]) was performed on 53 fracture planes for which kinematic data was obtained. These fractures are all part of interconnected fracture zones targeted by artisanal workers and are associated with the same sericite-sulphide alteration, and hence it is assumed that they formed simultaneously in response to the same far field stress. In doing the analysis all fracture planes were given the same weight (Appendix 1). Results are shown in figure 10, and indicate that $D_7$ shear zones in the central Kukuluma terrain formed in response to horizontal, NNE extension in a plane strain environment.

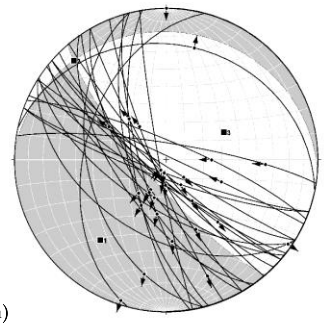

(a)

| *Axis* | *Eigenvalue* | *Trend* | *Plunge* |
|---|---|---|---|
| 1. ($\sigma_3$) | 0.3361 | 217.8, | 32.5 |
| 2. ($\sigma_2$) | 0.0356 | 315.7, | 12.2 |
| 3. ($\sigma_1$) | 0.3717 | 063.5, | 54.7 |

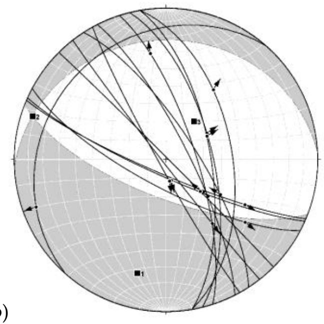

(b)

| *Axis* | *Eigenvalue* | *Trend* | *Plunge* |
|---|---|---|---|
| 1. ($\sigma_3$) | 0.2589 | 194.3, | 23.9 |
| 2. ($\sigma_2$) | 0.0660 | 288.0, | 08.3 |
| 3. ($\sigma_1$) | 0.1929 | 035.8, | 64.5 |

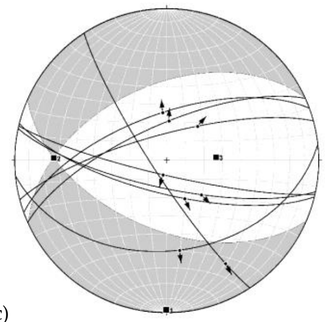

(c)

| *Axis* | *Eigenvalue* | *Trend* | *Plunge* |
|---|---|---|---|
| 1. ($\sigma_3$) | 0.3299 | 180.3, | 02.0 |
| 2. ($\sigma_2$) | 0.0011 | 271.3, | 26.4 |
| 3. ($\sigma_1$) | 0.3288 | 086.2, | 63.5 |

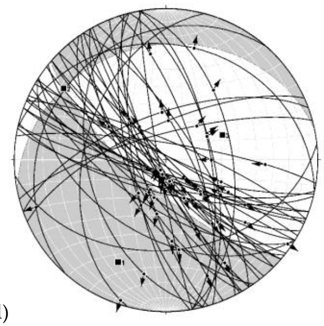

(d)

| *Axis* | *Eigenvalue* | *Trend* | *Plunge* |
|---|---|---|---|
| 1. ($\sigma_3$) | 0.2856 | 205.2, | 26.5 |
| 2. ($\sigma_2$) | 0.0261 | 304.9, | 18.7 |
| 3. ($\sigma_1$) | 0.3117 | 065.9, | 56.7 |

**Figure 10.** Orientation and palaeo-stress analysis for $D_7$ fracture arrays measured in Kukuluma and Matandani pits. For each area, the plot shows the fault planes as great circles and lineations as arrows that point in the direction of movement of the hanging wall; these are placed on top of the fault plane solution (Bingham matrix solution) for the measured $D_7$ faults (compression dihedron in white; tension dihedron in grey). The Bingham solutions for each data set are shown below the stereoplots. (a) W wall of Matandani pit (N = 30); (b) NE wall of Matandani pit (N = 13); (c) E wall of Kukuluma pit (N = 8); (d) all measurements from kukuluma and Matandani pits combined (N=51). All plots show N-S to NE-SW extension with a steep $\sigma_1$, and near horizontal $\sigma_2$ and $\sigma_3$ orientations.

Similar $D_7$ fractures are also targeted by artisanal miners in Area 3, where many are decorated by stringers of thin (<1cm wide) grey quartz containing visible gold. The larger scale distribution of the $D_7$ faults, beyond the pit areas, is not clear, because the structures are subtle and not exposed beyond the workings of artisanal miners.

## 4. The timing of intrusions and breccia formation during deformation

### *4.1. The emplacement of intrusions during deformation*

Deformation events were accompanied by the emplacement of two separate suites of syn-tectonic intrusions, one dioritic to monzonitic in composition, and a second granodioritic in composition that manifests itself as a first generation of porphyry dykes and sills. These intrusions are collectively called the Kukuluma Intrusive Complex (KIC; [27]) and they occur across the central part of the Kukuluma terrain (Fig. 3), where they were emplaced between 2715-2665 Ma [28]. They have been overprinted by a second generation of granodioritic porphyry dykes emplaced around 2650 Ma [28].

The diorite-monzonite suite of the KIC is dominated by equigranular, fine- to medium-grained, sheet-like bodies, stocks of diorite and plagioclase-rich porphyritic diorite dykes of irregular thickness (e.g. NW corner of Kukuluma pit), which locally form interconnected networks that both transect and parallel bedding (Fig. 3). The granodiorite suite comprises thin (<2 m wide) dykes with porphyritic textures that occur in a variety of orientations (steeply dipping dykes with W, NNW and N trends have been observed) [27].

The intrusive bodies belonging to the diorite-monzonite suite are weakly to moderately foliated as a result of $D_3$ deformation. In places intrusive margins and vein systems internal to the intrusions are folded during $D_3$ (e.g. 0418900-9687780). More commonly intrusions form sheet-like bodies that were emplaced along axial planar orientations of $D_3$ folds, with intrusive contacts cutting through ($D_3$) folded meta-sedimentary sequences, whilst foliations parallel to $S_3$ develop within the intrusions. In the SW part of Matandani pit, rafts of $D_3$ folded meta-ironstone occur within an intrusive diorite body that is foliated in an orientation parallel to $S_3$. Nowhere did we see diorite or monzonite intrusions being folded around $D_2$ structures, but the intrusions are affected by $D_4$ folding. Plagioclase-rich, porphyritic diorite dykes that form part of the diorite-monzonite suite cut through more massive diorite bodies, and are foliated. Where these dykes cut through meta-sediment, and especially $D_3$ planar high strain zones, they can be slightly folded as a result of $D_3$.

The field relationships indicate that the diorite-monzonite suite was emplaced after $D_2$, but immediately before and during $D_3$. The porphyritic granodiorite dykes of the KIC are not foliated and intrude into the diorite and monzonite bodies within Kukuluma and Matandani pits. The exact relationship of these dykes with $D_{5\text{-}6}$ shear zones is not clear, but they appear largely unaffected by these events. Two granodiorite dykes and a small granodiorite intrusion belonging to this suite of intrusion yield U-Pb zircon ages of 2667 ± 17 Ma, 2661 ± 16 Ma and 2663 ± 11 Ma [28].

A second generation of felsic porphyry dykes of granodioritic composition represented by a single, N-trending, 1-2 m wide, porphyritic felsic dyke transects Matandani pit (Fig. 3b). The dyke has chilled margins and no internal fabric and cuts through $D_1$-$D_6$ structures. Where this dyke cuts through the Juma and Kasata shears it can be seen to transect $D_6$ fabrics. However, the dyke is cut by narrow $D_7$ fracture planes, associated with slickensides, a sinistral normal sense of movement with limited displacement (<5 cm) and alteration including sulphide growth and gold mineralization, i.e. the timing of emplacement of this dyke is post $D_6$, but pre $D_7$ and pre-mineralization (Table 1). This dyke yields a zircon age of 2651 ± 14 Ma [28], which provides a maximum age constraint to mineralization.

*4.2. Syn-tectonic brecciation events*

Parts of the folded meta-sedimentary sequences in Kukuluma and Matandani pits have been brecciated. In Kukuluma pit, breccia zones are largely restricted to the W wall of the pit, and occur as elongated bodies, 5-50 m thick covering the entire height of the pit wall. They occur within the strongly $D_2$-$D_3$ folded package of meta-ironstone units with clasts consisting mostly of chert embedded in a more micaceous and feldspar-rich matrix, in close spatial association with intrusive dykes and stocks of the KIC. In Matandani pit, extensive brecciation occurs in the SW part of the pit, within strongly $D_2$-$D_3$ folded meta-ironstone intercalated with micaceous and graphitic shale, and concentrated along the W contact of a diorite intrusion that transects the centre of the pit (Fig. 3b). Outside the open pits, a major breccia body (~100 x 50 m in size) occurs to the NW of Matandani pit (Fig. 3a).

Breccia varies from crackle breccia, in which blocks have a jig-saw fit and the underlying folds and layering are preserved in a semi-coherent manner (Fig. 11a), to massive chaotic breccia in which the primary layering is destroyed (Fig. 11b). The change from jigsaw breccia to chaotic breccia is gradational, and along the W wall of Kukuluma pit, zones of more intense brecciation alternate with folded zones where brecciation is weak. Zones that display both $D_2$ and $D_3$ folds are brecciated, with some of the brecciation appearing more intense near fold hinge zones, i.e. in areas where the $S_3$, axial planar fracture cleavage was more intensely developed. Elsewhere (0418580-9688000; Fig. 11c), strongly brecciated layers in sharp contact with non-brecciated meta-ironstone are folded during $D_3$, indicating that some brecciation pre-dates $D_3$ folding and is strata-bound, possibly even indicating a syn-sedimentary origin for this breccia. The breccia zones are truncated by low angle reverse faults of $D_5$ origin and affected by $D_5$ recumbent folding. In areas where $D_5$ thrusts cut through the highly folded and fractured meta-ironstone units, brecciation also appears to occur in spatial association with the $D_5$ fault planes.

Zones of brecciation show a close spatial relationship with meta-ironstone units and dykes belonging to the KIC, with breccia occurring along the margins of intrusive diorite-monzonite bodies, or with dykes intruding into breccia zones. In one location (GR0418636-9687782; Fig.11e-h) a porphyritic diorite dyke intruded into the breccia and displays highly irregular boundaries, involving a planar trail of irregular, blob-like intrusive bodies up to 2 m in size with indented boundaries and irregular protrusions and apophyses of dyke material. This relationship suggests that the dyke was emplaced at the time the wall rocks had lost coherency as a result of brecciation; i.e. this dyke was emplaced at the same time as breccia formation. In Matandani pit a raft of crackle breccia, is embedded within a diorite intrusion with an $S_3$ foliation.

(a) (b)

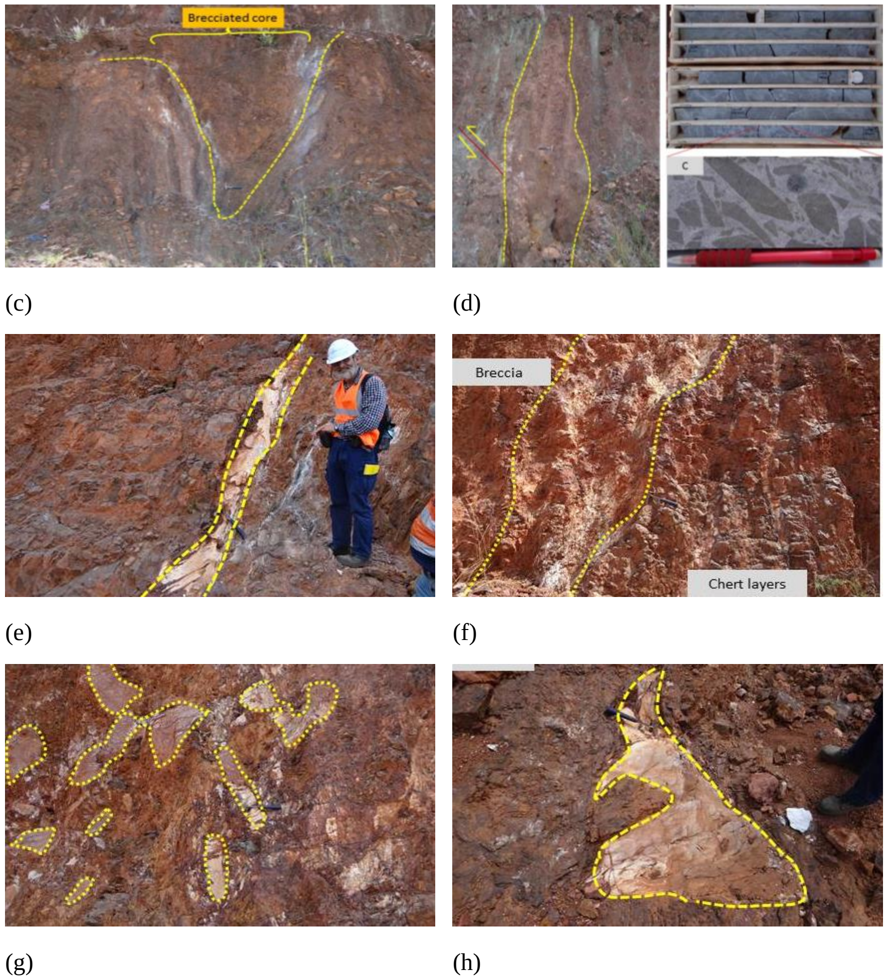


**Figure 11.** Examples of hydrothermal, syn-$D_3$ breccia and intrusions in Kukuluma pit: (a) and (b) progressive brecciation in meta-ironstones including a complexly folded zone with crackle breccia in which the original folded bedding is still visible (a) and more advanced brecciation in which individual clasts have moved, but remnants of underlying folds are visible (b); (c) layer-parallel breccia in the core of a $D_3$ fold; (d) fine-grained breccia pipe transecting a folded meta-ironstone package. The inset shows hydrothermal breccia in a diorite intrusive (drill hole ID: MTRD0005-588m); (e) and (f), diorite dyke (outlined with yellow stipple line) with highly irregular margins is emplaced into the breccia zone; (g) and (h) irregular blebs and fragments of diorite (outlined with yellow stipple line) mixed within the breccia near the intrusive contacts of the dyke shown in (e) and (f).

Locally (e.g. GR0418621-9687801), polymict breccia occurs with rare ~~green,~~ mafic clasts mixed with meta-ironstone clasts in chaotic breccia zones that transect folded meta-ironstone beds indicating considerable movement between breccia clasts. Locally the breccia bodies show a much higher degree of matrix material and a much smaller clast size along highly-altered, clay-rich planar zones that are reminiscent of fluid pathways in intrusive breccia pipes (Fig. 11d).

Based on available evidence, most breccia in Kukuluma and Matandani pits formed immediately preceding or during $D_3$, during the emplacement of the diorite and monzonite bodies to which they are spatially linked. They are best developed in the chert-rich meta-ironstone unit affected by $D_2$-$D_3$ folding. Although most brecciation appears to have been in-situ as a result of magmatic-~~,~~ hydrothermal activity, some 'streaming' of breccia blocks with pipe-like characteristics did occur.

Apart from the hydrothermal breccia associated with the KIC, there are planar breccia zones or cataclasite zones associated with $D_6$ shear zones (Fig. 5e), and syn-sedimentary chert clast breccias. The $D_6$ breccia zones are limited in areal extent and restricted to places where $D_6$ shear zones transect thick chert beds. Fragmental volcanoclastic sediments are common as intercalations within the meta-greywacke along the N wall of Kukuluma pit. These volcaniclastic rocks consist of strata-bound, matrix supported breccia layers with angular clasts and layer fragments of chert embedded in a matrix of arenitic sandstone. They differ from hydrothermal breccia in the proportion of clasts to matrix, the fact that some display grading and that they are stratabound.

## 5. Gold mineralization

The Kukuluma and Matandani deposits occur on a deeply weathered erosional plateau ~~that~~ interpreted to have formed part of the (Cretaceous) African Erosion Surface. Complete oxidation and weathering of all rock types occurs to depths of >100 m, and influenced gold distribution with leaching of gold in the top 20 m of the regolith profile, and supergene enrichment of gold near the base of the regolith [47]. The gold anomalies in Area 3 occur along the edge of the plateau, where the thick regolith has been largely removed by erosion.

Initial trenching of a weak soil anomaly in deeply weathered and leached rock in the Kukuluma-Matandani area gave few indications of the large ore bodies at depth, although, free "leaf" gold in old artisanal workings indicated gold was present. Exploration drilling revealed a general 2-3 g/t increase in mean grade between 60 and 105 m depth at Kukuluma and a planar zone of gold enrichment between the base of the regolith and the top of fresh rock [47]. Mining of the oxidized ore zones took place between 2002 and 2007, but once primary mineralization was reached mining stopped due to the refractory nature of the ore (arsenopyrite-rich with abundant graphite).

Gold mineralization is spatially related to: (a) competent lithologies, including meta-ironstone and chert that are distributed in a complex manner due to $D_2$-$D_3$-$D_4$ fold interference; (b) the locally brecciated, intrusive contacts between the ironstone and diorite and monzonite of the KIC; and (c) fracture networks of $D_6$ and $D_7$ origin (e.g. Fig. 12; [27]). The ore zones that consist mostly of disseminated mineralization, are generally tabular in shape with a NNW strike and steep dips, parallel to the contact zones of intrusions (Fig. 12). In Kukuluma pit it was observed that mineralization widens along the Juma shear where it cuts across the nose of an E plunging $D_3$ fold, and narrows again where the Juma shear runs oblique along the limbs of $D_3$ folds. A second ore zone in the pit occurs along the Kasata shear and is up to 50 m wide, trending 290°, where the Kasata shear intersects a complex $D_2$-$D_3$ antiformal fold interference structure in meta-ironstone; i.e. the presence of $D_3$ fold hinge zones appears to have affected the width of ore zones.

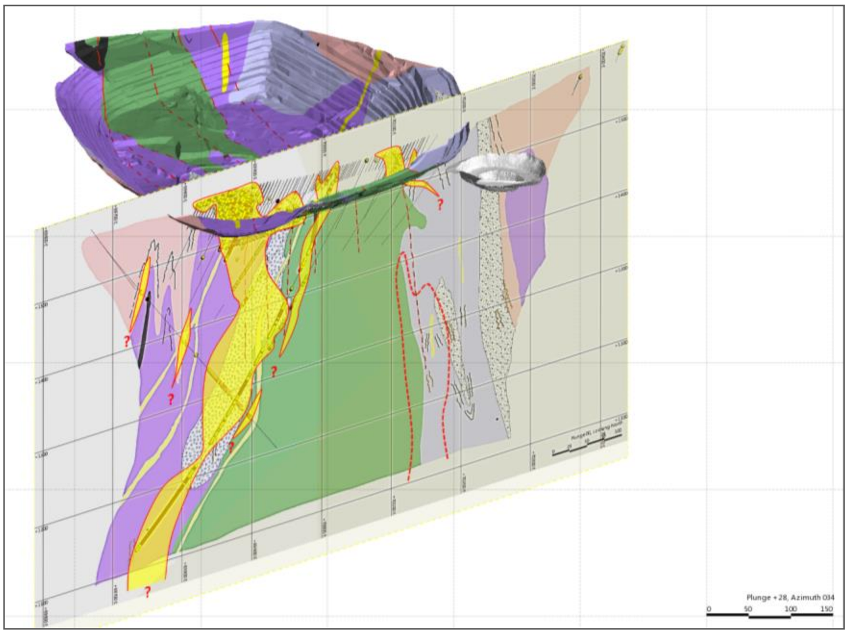


**Figure 12**. Example of a cross-section through Matandani pit showing the ore distribution along the margin of a dioritic body (green) in contact with meta-ironstone (purple) and breccia (stipple). Other units include interbedded meta-ironstone and greywacke (light blue) and volcaniclastics (pink). The inferred position of $D_6$ shear zones is shown with red stipple lines. The cut- off grade of ore envelope shown in yellow is 0.5 ppm. The section is vertical and trends 060 (right)-240 (left).

Direct observations of ore zones targeted by artisanal workers in Matandani and Kukuluma Pits, and Area 3 indicate that high grade ore zones occur along $D_7$ fracture planes, which locally parallel and reactivate portions of the Juma and Kasata shears. This relationship is clearly visible in the W part of Matandani pit where the main ore zone widens in a pocket of $D_2$-$D_3$ folded ironstone transected by two strands of the $D_6$, Kasata shear and overprinted by an ESE trending $D_7$ fracture zone. Sulphide mineralization in outcrop is spatially related to $D_7$ fracture planes and occurs in associated with grey to tan quartz stringers and sericite alteration. $D_7$ faulting and associated gold mineralization and alteration in Matandani pit postdates the emplacement of a granite dyke at 2651 ± 14 Ma [28], which itself transects the $D_6$ shear zones.

**Table 2.** (a) Length of logged drill core expressed in meters, listed by grade and rock type for the Matandani, Kukuluma and Area 3 West deposits. (b) Length of logged drill core expressed in % of total, listed by grade and rock type for the Matandani, Kukuluma and Area 3 West deposits. The lithological units listed comprise: Chert = massively banded chert and highly silicified laminated sedimentary units; Ironstone = well bedded, silicified, magnetite-rich units including BIF, transitional with chert; Volc = volcanoclastic units including agglomerate, fragmental tuff and ignimbrite; Seds =

sediments comprising alternating siltstone-shale units with layers of coarser-grained sandstone, grit and rare conglomerate; Bshale = graphitic black shale; Diorite = monzonite, and diorite of the Kukuluma Intrusive Complex.

| Deposit | grade | Chert | Ironstone | Volc | Seds | Bshale | Diorite | FP | Total |
|---|---|---|---|---|---|---|---|---|---|
| Matandani | >0.1 ppm Au (m) | **533.44** | **300.49** | **112.01** | **69.35** | **30.24** | **31.49** | **5.19** | **1082.21** |
| | >0.5 ppm Au (m) | **287.65** | **208.38** | **32.76** | **29.04** | **5.45** | **15.60** | **2.54** | **581.42** |
| | >1.0 ppm Au (m) | **193.59** | **174.70** | **20.04** | **18.64** | **1.50** | **15.60** | **0.00** | **424.07** |
| | >5.0 ppm Au (m) | **33.28** | **65.17** | **9.00** | **1.00** | **0.00** | **13.00** | **0.00** | **121.45** |
| Kukuluma | >0.1 ppm Au (m) | **175.79** | **283.07** | **73.07** | **92.11** | **17.97** | **40.47** | **0.00** | **682.48** |
| | >0.5 ppm Au (m) | **111.30** | **111.41** | **16.20** | **52.89** | **4.00** | **8.30** | **0.00** | **304.10** |
| | >1.0 ppm Au (m) | **86.65** | **45.98** | **3.00** | **41.75** | **3.00** | **4.30** | **0.00** | **184.68** |
| | >5.0 ppm Au (m) | **21.00** | **4.45** | **1.00** | **15.98** | **0.00** | **11.00** | **0.00** | **53.43** |
| Area 3 West | >0.1 ppm Au (m) | **127.75** | **265.34** | **49.86** | **7.00** | **17.35** | **17.00** | **0.00** | **484.30** |
| | >0.5 ppm Au (m) | **60.11** | **128.50** | **27.00** | **1.00** | **2.50** | **10.00** | **0.00** | **229.11** |
| | >1.0 ppm Au (m) | **37.36** | **93.34** | **12.70** | **0.00** | **0.00** | **4.00** | **0.00** | **147.40** |
| | >5.0 ppm Au (m) | **10.21** | **28.44** | **2.00** | **0.00** | **0.00** | **2.00** | **0.00** | **42.65** |

(a)

| Deposit | grade | Chert | Ironstone | Volc | Seds | Bshale | Diorite | FP | Total |
|---|---|---|---|---|---|---|---|---|---|
| Matandani | >0.1 ppm Au (%) | **49.29** | **27.77** | **10.35** | **6.41** | **2.79** | **2.91** | **0.48** | **100.00** |
| | >0.5 ppm Au (%) | **49.47** | **35.84** | **5.63** | **4.99** | **0.94** | **2.68** | **0.44** | **100.00** |
| | >1.0 ppm Au (%) | **45.65** | **41.20** | **4.73** | **4.40** | **0.35** | **3.68** | **0.00** | **100.00** |
| | >5.0 ppm Au (%) | **27.40** | **53.66** | **7.41** | **0.82** | **0.00** | **10.70** | **0.00** | **100.00** |
| Kukuluma | >0.1 ppm Au (%) | **25.76** | **41.48** | **10.71** | **13.50** | **2.63** | **5.93** | **0.00** | **100.00** |
| | >0.5 ppm Au (%) | **36.60** | **36.64** | **5.33** | **17.39** | **1.32** | **2.73** | **0.00** | **100.00** |
| | >1.0 ppm Au (%) | **46.92** | **24.90** | **1.62** | **22.61** | **1.62** | **2.33** | **0.00** | **100.00** |
| | >5.0 ppm Au (%) | **39.30** | **8.33** | **1.87** | **29.91** | **0.00** | **20.59** | **0.00** | **100.00** |
| Area 3 West | >0.1 ppm Au (%) | **26.38** | **54.79** | **10.30** | **1.45** | **3.58** | **3.51** | **0.00** | **100.00** |
| | >0.5 ppm Au (%) | **26.24** | **56.09** | **11.78** | **0.44** | **1.09** | **4.36** | **0.00** | **100.00** |
| | >1.0 ppm Au (%) | **25.35** | **63.32** | **8.62** | **0.00** | **0.00** | **2.71** | **0.00** | **100.00** |
| | >5.0 ppm Au (%) | **23.94** | **66.68** | **4.69** | **0.00** | **0.00** | **4.69** | **0.00** | **100.00** |

(b)

Higher grade ore in the Matandani, Kukuluma and Area 3 deposits is normally found within meta-ironstone and chert units, with low-grade ore distributed over a larger range of lithologies (Table. 2, Fig. 12). For 30 diamond drill holes, representing a total length of 6094 m from Matandani (2160 m), Kukuluma (1787 m) and Area 3 (2147 m), which transect the main ore zones, the total length of mineralized rock at grades of >0.1, >0.5, >1 and >5 ppm gold was measured as a function of rock type. It was noted that rocks were not always logged in the same manner, so that generalizations had to be made. All deposits show similar relationships between host lithology and ore grade, with >75% of high-grade material (>5 ppm) hosted in grunerite-magnetite-chlorite-biotite-rich meta-ironstone and chert units (81% at Matandani, 73% at Kukuluma and 82% at Area 3; Table 2), suggesting a close relationship between mechanically competent, iron-rich lithologies and gold mineralization.

Significant high-grade mineralization also occurs in sedimentary units (30% at Kukuluma) and in the monzodiorite~~-diorite intrusions~~ (11% at Matandani, 21% at Kukuluma and 5% at Area 3; Table 2). The ~~monzonite-diorite intrusions~~latter are generally mineralized to within ~3 m from the contact with mineralized meta-ironstone, especially near zones where the margin is sheared and meta-ironstone xenoliths occur within the intrusions. At lower grades (<1 ppm), other lithologies host some mineralization, but the bulk of the ore (~70-80%) continues to be hosted in the highly fractured, silicified meta-ironstone and chert lithologies (Table 2).

Gold in fresh meta-ironstone is fine-grained (<20 µm) and occurs preferentially ~~within~~ as inclusions in magnetite, pyrrhotite, pyrite and arsenopyrite grains that are spatially associated with fibrous grunerite aggregates, silicification and chlorite-biotite alteration. Grunerite is not restricted to ore zones, but is also a regional metamorphic mineral that formed during $D_2$-$D_3$ events. In mineralized zones magnetite is replaced by pyrrhotite, and arsenopyrite-pyrrhotite-pyrite-stibnite-scheelite assemblages occur in fracture networks and as disseminations associated with gold. The alteration assemblage affects intrusive units of the KIC at or near the sheared contact zones (Fig. 12). Higher grades are recorded in areas where arsenopyrite is dominant and chlorite alteration less prominent. In highly mineralized zones gold is associated with a network of mm-scale micro-fractures, probably of $D_7$ origin, that are in-filled with pyrrhotite and arsenopyrite, and that are best develop in chert-rich layers of brecciated and folded meta-ironstone units. High-grade gold mineralization has also been observed in breccia zones that are not obviously ($D_6$) sheared, but that are close to shears and occur next to the contact with the diorite and monzonite intrusives. In such areas, intense micro-fracturing can be observed in drill core with progressive infill of pyrrhotite in fractures within the ore zone.

## 6. Discussion

### *6.1. Tectonic and magmatic history of the central Kukuluma terrain.*

A summary of the deformation, intrusive and mineralizing events encountered in the central part of the Kukuluma terrain is presented in Table 1. The deformation events in the Kukuluma-Matandani area comprise 3 groups of structures that formed during 3 separate stages in the ~~geodynamic~~ tectonic history of the belt. These groups are: (a) $D_1$ structures that formed during Stage 1, extensional deformation, which involved small-scale, syn-sedimentary growth faulting, layer-parallel shearing with silicification and stratigraphic attenuation. $D_1$ structures formed at the time of sedimentation and early volcanism around 2717 ± 12 Ma, in an oceanic plateau environment [28]; (b) Penetrative structures ($D_2$-$D_6$) that involved overprinting folding, shearing and brecciation events during the main compressional Stage 2 of deformation, including an early episode of upright folding ($D_2$) followed by distributed shearing and cylindrical upright folding with NW trending axial planar surfaces ($D_3$), overprinted by open vertical folding ($D_4$) and then recumbent folding and thrusting ($D_5$) in response to N-S shortening. This was followed by the development of a network of brittle-ductile shear zones recording reverse movements consistent with continued N-S shortening ($D_6$; Fig. 9), all happening before the emplacement of a set of felsic dykes around 2665 Ma as a result of the Geita greenstone terrain docking against an older cratonic terrain to the S [28,39]; and (c) Localized $D_7$ structures that formed during Stage 3 extensional deformation (Fig. 10), when strain was partitioned into discrete normal faults and joints ($D_7$) at some time after 2650 Ma [28], during the stabilization phase of the craton [30].

Deformation events were accompanied by the emplacement of a diorite-monzonite suite that largely intruded during $D_3$, and a granodiorite suite (mostly dykes) that intruded around 2665 Ma [28], probably after $D_6$. Collectively these intrusions form the Kukuluma Intrusive Complex (KIC, [27]). Rocks of the KIC have an adakite-like signature, but the trace element geochemistry and very narrow variation in Th/U ratios is inconsistent with a subduction origin [27]. It has, therefore, been proposed that the KIC~~, which~~ formed by partial melting of garnet-bearing, mafic crust at the base of ~~resulted from intra-crustal melting at the base of~~ a thickened oceanic plateau, and ~~may not have~~did not involve~~d~~ subduction [27], similar to other volcanic units in the area [37] and mafic-felsic crust in other greenstone belts [22,51-53] [54].

The intrusions of the KIC are spatially associated with breccia bodies that formed along intrusive margins with meta-ironstone units. Late-tectonic felsic porphyry dykes cross-cut all units and $D_1$-$D_6$ structures, and one such dyke, which is cut by D7 faults, has been mineralized and dated at 2651 ± 14 Ma [28]. This dyke provides an upper age constraint for gold mineralization in the area. With respect to gold mineralization, the ductile group of compressional $D_{2-6}$ structures created the architecture that influenced the distribution of rock-types favorable for gold precipitation, whereas the $D_7$ faults appear to have controlled fluid infiltration, which would have been facilitated by the extensional environment in which these structures formed [14] [8,20].

The deformation and intrusive sequence of events described for the gold deposits in the Kukuluma terrain (Table 1) is near-identical to the deformation-intrusive sequences ~~obtained~~ described in the Nyankanga [11] and Geita Hill [26] deposits in the Central terrain, even though the latter occur across a major shear zone at somewhat lower peak metamorphic conditions (Fig. 2). Both areas record early $D_1$ events associated with syn-sedimentary extensional faulting and chert formation along discordant zones. $D_{2-4}$ events in both areas are near identical, with the exception that $D_{2-4}$ structures in the Kukuluma terrain preserve a greater diversity in fold-axes orientation. Unlike the Nyankanga-Geita Hill area, the central parts of the Kukuluma terrain also preserves localized, planar $D_3$ high strain zones with NW plunging lineations in which $S_0$, $S_1$, $S_2$ and $S_3$ fabrics have been transposed.

$D_5$ events in the Kukuluma pit area are more clearly developed than at Geita Hill or Nyankanga [11,26], with recumbent folding showing a clear relationship with low-angle reverse faults. Such structures are common in greenstone belts, and may have resulted from the rise of diapirs and consequent steepening of the margins of the greenstone belt [55,56].

$D_6$ brittle-ductile shears in the Kukuluma terrain correlate to the N-dipping sinistral thrust zones in Nyankanga and Geita Hill; they are identical in metamorphic grade and only vary in orientation and dominant shear sense, but both are consistent with N-S shortening [26]. In the Kukuluma and Matandani pits, the network of $D_6$ shear zones share a common, steeply WNW plunging (Fig. 10) intersection lineation that more-or-less parallels $D_4$ fold axes, a dominant cluster of $D_3$ fold axes (Fig. 6d) and the mineral elongation lineation in $D_3$ high strain zones. This co-linearity of deformation features was also noted in the Geita Hill deposit [26] where mineralization followed the same general trend, and it has been interpreted to reflect a co-genetic relationship of $D_2$-$D_6$ events linked to the same large-scale compressional processes [11,26,57].

**Formatted:** Left, Hyphenate, Don't adjust space between Latin and Asian text, Don't adjust space between Asian text and numbers

**Formatted:** Subscript

Later reactivation of $D_6$ shears in Geita Hill and Nyankanga involved several events including strike-slip and normal movements grouped as $D_{7-8}$ events, whilst in the central Kukuluma terrain these events are grouped as $D_7$ with normal movement being dominant. In both areas the late extensional events are spatially and temporally associated with gold mineralization that occurred after 2650 Ma [26,35].

~~Similar~~In parallel with ~~to~~ the deformation sequence, the intrusive rocks of the KIC correlate~~s~~ in composition and relative timing with the Nyankanga Intrusive Complex [27,28,30], and both areas show evidence of igneous events associated with felsic dykes and lamprophyres that were emplaced after $D_6$ and before $D_7$.

The similarity in the deformation-intrusive histories for the Central and Kukuluma terrains suggests that the tectonic history for much of the GGB is similar, and that terrain boundaries internal to the GGB do not separate diverse domains as ~~would be expected~~has been suggested in accretionary terranes [10,17,58]. It also means that age constraints obtained from the Nyankanga-Geita area can probably be applied to the Kukuluma-Matandani area and vice versa. Thus, $D_{1-6}$ events near Kukuluma probably occurred at the same time as $D_{1-6}$ events at Geita Hill [11,39], i.e. between 2720 and 2660 Ma including the emplacement of the KIC, which by comparison with the Nyankanga Intrusive Complex may have occurred between 2700-2685 Ma [26,35]. A date of 2717 ± 12 Ma for syn-sedimentary volcanics from Kukuluma Pit [28] provides an estimate for the timing of extensional $D_1$ events. Compressional $D_{2-4}$ events at Nyankanga and Geita pits are constrained to 2700-2675 Ma [11,35], whilst $D_{5-6}$ events represent a later retrograde compressional stage of deformation, possibly at 2675-2660 Ma as suggested by the ages obtained for the granodiorite dykes of the KIC [27,28]. A late granodiorite dyke in Matandani pit constrains the timing of $D_7$ normal faulting and mineralization to <2650 Ma, consistent with observations in Geita Hill where mineralization is <2644 Ma [26,35], which also coincided with the emplacement of 2620-2660 Ma granitoids to the E, N and W of the GGB [30].

*6.2. Controls on gold mineralization*

Spatially, gold mineralization within the Kukuluma and Matandani deposits is associated with $D_{6,7}$ shear zones located along the contact zone between diorite intrusions of the KIC and magnetite-rich, meta-ironstone units within the surrounding volcano sedimentary package (e.g. Fig. 12). High-grade mineralization is also closely associated with networks of extensional $D_7$ fractures, where they occur in ironstone~~s~~ and metasediment~~s~~ away from $D_6$ shear zones. Ore zones occur almost entirely within the meta-ironstone units, and differ in this respect from mineralization in Nyankanga and Geita Hill, where diorite of the Nyankanga Intrusive Complex is widely mineralized, be it at a lower grade [11,25,41]. The ore zones widen where $D_{6,7}$ shear zones traverse intensely folded and highly brecciated areas. $D_3$ fold axial zones and syn-$D_3$ hydrothermal breccia zones near KIC intrusive margins were especially conducive to the infiltration of mineralizing fluids, which ~~entered~~ infiltrated the rock along pre-existing micro-fracture networks. However, this relationship only holds where mineralized $D_6$ shear zones are in close proximity to the folded and brecciated areas; i.e. brecciation of meta-ironstone units in itself does not guarantee gold mineralization. These relationships indicate that the $D_7$ fracture zones in the Matandani-Kukuluma area acted as upper-crustal channels for the mineralizing fluids, facilitating the infiltration into fractured zones offered by the strongly folded and brecciated meta-ironstones [59]. In this context it is important to note that the distribution of the meta-ironstone units is highly complex as a result of $D_{2\text{-}4}$ fold interference, and, therefore, that the intersection zones of $D_{2\text{-}4}$ folded ironstones and $D_{6,7}$ shears and fracture zones is highly discontinuous, which contributes to the complex distribution patterns of the ore zones in the area.

Earlier mine reports argued that mineralization was controlled by the Juma and Kasata shears (Fig. 3), and that their apparent displacement between Kukuluma and Matandani pits was the result of later E-W, sinistral faults. A similar E-W fault was assumed to have displaced the S end of the Juma shear to account for mineralization in Area 3 to the E [60] [48]. Pit exposure, shows that the Juma and Kasata shears anastomose and change in orientation from W-trending to NW trending, with no evidence for offsets by later E-W faults. Likewise the E tip of the Juma fault displays a complex fault splay, characteristic for fault tips or terminations [46], with no evidence of displacement by cross cutting faults. The Juma and Kasata shears do, however, show evidence for an earlier, $D_6$ compressional stage, overprinted by a later, $D_7$ extensional stage; and the late E-W fracture zones identified by [48] represent the cross cutting $D_7$ structures reported here that are associated with hydrothermal alteration, but have no major displacements. Thus, the spaced distribution of mineralization from Area 3, via Kukuluma to Matandani should be understood in terms of an en echelon array along a WNW trending corridor, rather than a continuous NW trending ore zone displaced by later E-W faults. This en echelon array of faults did not accommodate large displacements, neither during $D_6$ nor $D_7$, because the strike length of the faults is generally < 500 m [61,62]. The en echelon array probably originally formed in compression during $D_6$ and was reactivated and partly overprinted by normal faults during $D_7$, which developed along E-W corridors [26,48], and possibly visible as E-trending lineaments in geophysical data sets. Even though displacements would have been small, fluid ascent and penetration could have been highly effective during $D_7$ extension, as a small shift in the far-field stress could have greatly enhanced permeability of pre-existing micro-fracture networks and facilitated improved fluid-rock interactions [59,63] [14,64-66]. In this context it is important to note that the ore zones in Kukuluma and Matandani pits widen, where the $D_{6,7}$ shear zones display S-like bends (from NW to W to NW trending). Such S-bends would be constraining bends [46] during $D_6$ reverse faulting, but would be areas of maximum dilatancy during $D_7$ [9,14,63]. The drop in fluid pressure and possibly temperature that would have occurred along the micro-fracture zones in extension would also have played a role in ore deposition [14].

The close spatial relationship of gold with meta-ironstone and the intrusive margins of the KIC indicate a litho-chemical control on mineralization with sulphidation of the magnetite-rich units being particularly important. It is, therefore, assumed that much of the gold entered the system as sulphur complexes, which destabilized upon contact with Fe-rich lithologies, i.e. magnetite-rich units [11,67-71]. Compared to other major deposits in the GGB, mineralization in Kukuluma and Matandani is more pyrrhotite-arsenopyrite-rich, which may reflect a combination of higher metamorphic grade, reduced conditions due to the presence of graphitic shale and host-rock control. The presence of porphyry dykes in association with mineralization, not just in Matandani pit, but also at Geita Hill [26] and Nyankanga [11] would suggest that igneous fluids may have caused mineralization, even though in Archaean Greenstone terrains more broadly, devolatization reactions during regional metamorphism are generally credited as being the primary source for mineralizing fluids [3,8,70]**.** It is beyond the scope of this paper to fully discuss the origin of gold-bearing fluids, which will require additional isotopic and fluid inclusion studies.

In terms of timing of gold mineralization in the Kukuluma terrain, the situation is similar to the Geita Hill and Nyankanga deposits, with mineralization spatially linked to $D_2$-$D_3$ fold noses and $D_6$ reverse faults that formed during the compressional stages of the deformation history [11]. The mineralizing event (i.e. $D_8$ at Nyankanga and Geita Hill [11,26], $D_7$ at Matandani-Kukuluma; Table 1), however, is late-tectonic and associated with normal fault reactivation of the older reverse faults. The mineralizing events post-date an intrusive event dated at 2651 Ma in the Matandani pit [28] and at 2644 Ma in the Geita Hill deposit [35], where lamphrophyre dykes occur in association with mineralization [26,35]. Thus, whilst the ore-body geometries are entirely controlled by deformational geometries and lithological distributions that formed during the stage 2 (i.e. ~2700-2665 Ma) evolution of the GGB, the actual mineralizing events probably occurred later when fluids, possibly linked to a deeper igneous source, moved into the dilatant zones during extension [9,11,26]. A similar, relative timing relationship of deformation structures, intrusions and gold mineralization also exists in other parts of the Tanzania Craton ([72-74]; e.g. in the Golden Pride deposit, in the Nzega Greenstone Belt (Fig. 1), mineralization was introduced along a crustal scale shear zone during late-stage reactivation, and accompanied by the intrusion of lamprophyre and quartz porphyry dykes. Mineralization was concentrated along late cross-cutting fractures near redox fronts provided by BIF's [74].

The structural controls on gold mineralization at Kukuluma and Matandani conform with models for Archaean gold mineralization more broadly as summarized by [9] and~~–~~ [8] in the sense that mineralization is late-tectonic, appears to occur as a single event during a shift in the far field stress, precedes cratonic stabilization and is associated with a range of structural traps created earlier in the deformation and intrusive history of the belt. However, the Kukuluma, Matandani and Area 3 deposits do not fit the orogenic model as defined by [9,70] or [2]. In review papers on gold mineralization the Geita mine is commonly classified as a Neoarchaean, BIF-hosted, orogenic gold deposit [1-3,6,7] related to subduction-accretion systems with all mafic sequences deposited in a subduction-back arc environment [10,36]. More recent work [11,26,37,39] shows that this interpretation needs adjustment. Rather than forming in a classic orogenic setting, mineralization entered the greenstone belt during an extensional phase concomitant with the emplacement of widespread high-K granites [30], ~20-30 Ma after compressional deformation and accretion of the greenstone sequence. The mafic-intermediate volcanics in the GGB ~~could have~~ evolved from melt segregation of a primitive mantle ~~below~~ to form thick oceanic plateaus away from subduction systems and accretionary margins [37,39]. Compressional deformation events coincided with the emplacement of diorite-monzonite complexes like the KIC that formed from partial melting of garnet-bearing~~,~~ mafic crust at the base of the oceanic plateaus, suggesting that ~~and~~ the greenstone sequence may ~~in fact~~ have never experienced accretion-subduction processes as postulated by earlier workers [10]. If so, this would invalidate a traditional orogenic setting for the gold deposits in the GGB [1].

## 7. Conclusions

Detailed mapping of the central part of the Kukuluma terrain in the eastern GGB shows that the deformation-intrusive history of the area (Table 1) is near identical to the geological history of the

Central terrain, which hosts the world class Nyankanga and Geita Hill deposits. This similarity occurs across major shear zones, and suggests that the geological history of much of the GGB is similar, with syn-sedimentary extension ($D_1$) followed by an early compressional-accretionary stage ($D_{2\text{-}6}$) between 2700-2665 Ma associated with the emplacement of internal intrusions of the KIC, and a later extensional stage ($D_7$) associated with a second generation of felsic intrusions, and gold mineralization ~~which~~ that occurred after 2650 Ma.

The geometry of the ore bodies at Kukuluma and Matandani is controlled by the distribution of magnetite-rich meta-ironstone, near the margins of monzonite-diorite bodies of the KIC where they are cut by $D_7$ fractures. The lithological contacts act as redox boundaries, with high-grade mineralization enhanced in zones of improved permeability and fluid infiltration including syn-$D_3$ hydrothermal breccia zones, $D_2$-$D_3$ fold hinge domains associated with a high density of micro-fracturing and $D_6$ shears with associated damage zones. The actual mineralizing events were late-tectonic (<2650 Ma), and occurred in an extensional setting during $D_7$. Extension facilitated the infiltration of mineralizing fluids along pre-existing micro-fracture networks of $D_2$-$D_6$ origin, as well as $D_7$ deformation zones.

The Kukuluma and Matandani deposits provide excellent examples of complex trapping structures that formed as a result of multiple overprinting deformation events before the gold was introduced [9]. Thus, whilst gold mineralization is late-tectonic, ore body geometries are associated with older structures and lithological boundaries.

In the GGB, deformation and intrusive sequences on outcrop scale are similar to other greenstone belts. However, the major gold deposits in the GGB lack the proximity of crustal-scale shear zones, are associated with intrusive complexes like the KIC, do not show a clear link to a subduction-accretion setting and formed late-tectonically during an extensional phase. These deposits are not characteristic of typical orogenic gold deposits.

**Acknowledgments:** This study is part of a PhD study undertaken by the first author at James Cook University. SDK would like to thank James Cook University for waiving the tuition fees and Geita Gold Mine for providing the research funding for this study.

**Author Contributions:** S.D.K, P.D, I.S, T.B and SK have conceived, designed the project and performed the field work; S.D.K and P.D. analysed the data; S.D.K, P.D. and I.S. wrote the paper.

**Conflicts of Interest:** The authors declare no conflict of interest.

## References

***1.*** ***Goldfarb, R.J.; Groves, D.I.; Gardoll, S. Orogenic gold and geologic time: A global synthesis. Ore Geology Reviews 2001, 18, 1-75.***

***2.*** ***Goldfarb, R.J.; Baker, T.; Dube, B.; Groves, D.; Hart, C.; Gosslein, P. Distribution, character and genesis of gold deposits in metamorphic terranes. In Economic geology one hundredth anniversary volume, Society of Economic Geologists, Inc.: 2005; pp 407-450.***

***3.*** ***Groves, D.I.; Vielreicher, R.M.; Goldfarb, R.J.; Condie, K.C. Controls on the heterogeneous distribution of mineral deposits through time. Geological Society, London, Special Publications 2005, 248, 71-101.***

***4.*** ***Laznicka, P. Giant metallic deposits—a century of progress. Ore Geology Reviews 2014, 62, 259-314.***
***5.*** ***Groves, D.I.; Goldfarb, R.J.; Gebre-Mariam, M.; Hagemann, S.G.; Robert, F. Orogenic gold deposits: A proposed classification in the context of their crustal distribution and relationship to other gold deposit types. Ore Geology Reviews 1998, 13, 7-27.***
***6.*** ***Bierlein, F.P.; Groves, D.I.; Cawood, P.A. Metallogeny of accretionary orogens — the connection between lithospheric processes and metal endowment. Ore Geology Reviews 2009, 36, 282-292.***
***7.*** ***Bierlein, F.P.; Groves, D.I.; Goldfarb, R.J.; Dubé, B. Lithospheric controls on the formation of provinces hosting giant orogenic gold deposits. Mineralium Deposita 2006, 40, 874-886.***
***8.*** ***Goldfarb, R.J.; Groves, D.I. Orogenic gold: Common or evolving fluid and metal sources through time. Lithos 2015, 233, 2-26.***
***9.*** ***Groves, D.I.; Santosh, M.; Goldfarb, R.J.; Zhang, L. Structural geometry of orogenic gold deposits: Implications for exploration of world-class and giant deposits. Geoscience Frontiers 2018.***
***10.*** ***Kabete, J.M.; Groves, D.I.; McNaughton, N.J.; Mruma, A.H. A new tectonic and temporal framework for the tanzanian shield: Implications for gold metallogeny and undiscovered endowment. Ore Geology Reviews 2012, 48, 88-124.***
***11.*** ***Sanislav, I.V.; Kolling, S.L.; Brayshaw, M.; Cook, Y.A.; Dirks, P.H.G.M.; Blenkinsop, T.G.; Mturi, M.I.; Ruhega, R. The geology of the giant nyankanga gold deposit, geita greenstone belt, tanzania. Ore Geology Reviews 2015, 69, 1-16.***
***12.*** ***Frimmel, H.E. Earth's continental crustal gold endowment. Earth and Planetary Science Letters 2008, 267, 45-55.***
***13.*** ***Sibson, R.H. Controls on maximum fluid overpressure defining conditions for mesozonal mineralisation. Journal of Structural Geology 2004, 26, 1127-1136.***
***14.*** ***Cox, S.F. Coupling between deformation, fluid pressures, and fluid flow in ore-producing hydrothermal systems at depth in the crust. In One hundredth anniversary volume, Hedenquist, J.W.; Thompson, J.F.H.; Goldfarb, R.J.; Richards, J.P., Eds. Society of Economic Geologists: 2005.***
***15.*** ***Robert, F.; Poulsen, K.H.; Cassidy, K.F.; Hodgson, C.J. Gold metallogeny of the superior and yilgarn cratons. In One hundredth anniversary volume, Hedenquist, J.W.; Thompson, J.F.H.; Goldfarb, R.J.; Richards, J.P., Eds. Society of Economic Geologists: 2005.***
***16.*** ***Bateman, R.; Hagemann, S. Gold mineralisation throughout about 45 ma of archaean orogenesis: Protracted flux of gold in the golden mile, yilgarn craton, western australia. Mineralium Deposita 2004, 39, 536-559.***
***17.*** ***Blewett, R.S.; Henson, P.A.; Roy, I.G.; Champion, D.C.; Cassidy, K.F. Scale-integrated architecture of a world-class gold mineral system: The archaean eastern yilgarn craton, western australia. Precambrian Research 2010, 183, 230-250.***
***18.*** ***Baker, T.; Bertelli, M.; Blenkinsop, T.; Cleverley, J.S.; McLellan, J.; Nugus, M.; Gillen, D. P-t-x conditions of fluids in the sunrise dam gold deposit, western***

***australia, and implications for the interplay between deformation and fluids. Economic Geology 2010, 105, 873-894.***

***19. Jones, S. Contrasting structural styles of gold deposits in the leonora domain: Evidence for early gold deposition, eastern goldfields, western australia. Australian Journal of Earth Sciences 2014, 61, 881-917.***

***20. Dirks, P.H.G.M.; Charlesworth, E.G.; Munyai, M.R.; Wormald, R. Stress analysis, post-orogenic extension and 3.01ga gold mineralisation in the barberton greenstone belt, south africa. Precambrian Research 2013, 226, 157-184.***

***21. Bédard, J.H.; Brouillette, P.; Madore, L.; Berclaz, A. Archaean cratonization and deformation in the northern superior province, canada: An evaluation of plate tectonic versus vertical tectonic models. Precambrian Research 2003, 127, 61-87.***

***22. Bédard, J.H. A catalytic delamination-driven model for coupled genesis of archaean crust and sub-continental lithospheric mantle. Geochimica et Cosmochimica Acta 2006, 70, 1188-1214.***

***23. Hamilton, W.B. Plate tectonics began in neoproterozoic time, and plumes from deep mantle have never operated. Lithos 2011, 123, 1-20.***

***24. Van Kranendonk, M.J. Cool greenstone drips and the role of partial convective overturn in barberton greenstone belt evolution. Journal of African Earth Sciences 2011, 60, 346-352.***

***25. Borg, G. The geita gold deposit, nw-tanzania. Geology, ore petrology, geochemistry and timing of events. Geol. Jahrb. 1994, D100, 545-595.***

***26. Sanislav, I.V.; Brayshaw, M.; Kolling, S.L.; Dirks, P.H.G.M.; Cook, Y.A.; Blenkinsop, T.G. The structural history and mineralization controls of the world-class geita hill gold deposit, geita greenstone belt, tanzania. Mineralium Deposita 2017, 52, 257-279.***

***27. Kwelwa, S.D.; Sanislav, I.V.; Dirks, P.H.G.M.; Blenkinsop, T.; Kolling, S.L. The petrogenesis of the neoarchean kukuluma intrusive complex, nw tanzania. Precambrian Research 2018, 305, 64-78.***

***28. Kwelwa, S.D.; Sanislav, I.V.; Dirks, P.H.G.M.; Blenkinsop, T.; Kolling, S.L. Zircon u-pb ages and hf isotope data from the kukuluma terrain of the geita greenstone belt, tanzania craton: Implications for stratigraphy, crustal growth and timing of gold mineralization. Journal of African Earth Sciences 2018, 139, 38-54.***

***29. Sanislav, I.V.; Dirks, P.H.G.M.; Blenkinsop, T.; Kolling, S.L. The tectonic history of a crustal-scale shear zone in the tanzania craton from the geita greenstone belt, nw-tanzania craton. Precambrian Research 2018, 310, 1-16.***

***30. Sanislav, I.V.; Wormald, R.J.; Dirks, P.H.G.M.; Blenkinsop, T.G.; Salamba, L.; Joseph, D. Zircon u–pb ages and lu–hf isotope systematics from late-tectonic granites, geita greenstone belt: Implications for crustal growth of the tanzania craton. Precambrian Research 2014, 242, 187-204.***

***31. Gabert, G. Lithostratigraphic and tectonic setting of gold mineralization in the archean cratons of tanzania and uganda, east africa. Precambrian Research 1990, 46, 59-69.***

***32.*** ***Kuehn, S.; Ogola, J.; Sango, P. Regional setting and nature of gold mineralization in tanzania and southwest kenya. Precambrian Research 1990, 46, 71-82.***

***33.*** ***Borg, G. New aspects of the lithostratigraphy and evolution of the siga hills, an archaean granite-greenstone terrain in nw tanzania. Zeitschrift fur Angewandte Geologie 1992, 38, 89-93.***

***34.*** ***Borg, G.; Shackleton, R.M. The tanzania and ne-zaire cratons. Oxford University Press: Oxford, 1997.***

***35.*** ***Borg, G.; Krogh, T. Isotopic age data of single zircons from the archaæan sukumaland greenstone belt, tanzania. Journal of African Earth Sciences 1999, 29, 301-312.***

***36.*** ***Manya, S.; Maboko, M.A.H. Geochemistry of the neoarchaean mafic volcanic rocks of the geita area, nw tanzania: Implications for stratigraphical relationships in the sukumaland greenstone belt. Journal of African Earth Sciences 2008, 52, 152-160.***

***37.*** ***Cook, Y.A.; Sanislav, I.V.; Hammerli, J.; Blenkinsop, T.G.; Dirks, P.H.G.M. A primitive mantle source for the neoarchean mafic rocks from the tanzania craton. Geoscience Frontiers 2016, 7, 911-926.***

***38.*** ***Kabete, J.M.; McNaughton, N.J.; Groves, D.I.; Mruma, A.H. Reconnaissance shrimp u–pb zircon geochronology of the tanzania craton: Evidence for neoarchean granitoid–greenstone belts in the central tanzania region and the southern east african orogen. Precambrian Research 2012, 216-219, 232-266.***

***39.*** ***Sanislav, I.V.; Blenkinsop, T.G.; Dirks, P.H.G.M. Archean crustal growth through successive partial melting events in an oceanic plateau-like setting in the tanzania craton. Terra Nova 2018, 0, 1-10.***

***40.*** ***Manya, S. Petrogenesis and emplacement of the ttg and k-rich granites at the buzwagi gold mine, northern tanzania: Implications for the timing of gold mineralization. Lithos 2016, 256-257, 26-40.***

***41.*** ***Borg, G.; Lyatuu, D.R.; Rammlmair, D. Genetic aspects of the geita and jubilee reef archean bif-hosted gold deposits, tanzania. Geologische Rundschau 1990, 79, 355-371.***

***42.*** ***Skead, M.B.; Chuwa, G. Geita west deposit – geological and mineralization model. Internal AngloGold report, Geita Gold Mine - Exploration Departmen 2003, 26.***

***43.*** ***Painter, M. Mineralisation and structural architecture of the geita hill shear zone. Internal AngloGold Report, Geita Gold Mine 2004, 26.***

***44.*** ***Hofmann, A.; Dirks, P.H.G.M.; Jelsma, H.A. Late archaean foreland basin deposits, belingwe greenstone belt, zimbabwe. Sedimentary Geology 2001, 141-142, 131-168.***

***45.*** ***Thiessen, R. Two-dimensional refold interference patterns. Journal of Structural Geology 1986, 8, 563-573.***

***46.*** ***Fossen, H. Structural geology. Cambridge University Press: Cambridge, 2010.***

***47.*** ***Bansah, D.; Chase, R.; Davidson, A.; Michael, H.; Skead, M. The geita and kukuluma mineralized trends, lake victoria goldfield, tanzania – ore body***

***characteristics and project planning. Proceedings of the 4th International Mining Geology Conference, Coolum, Qld 2000, 115-127.***

48. ***Skead, M.B. Geology and structure of the kukuluma deposit, geita greenstone belt, tanzania. Internal AngloGold report, Geita Gold Mine 2003, 27.***
49. ***Marrett, R.; Allmendinger, R.W. Kinematic analysis of fault-slip data. Journal of Structural Geology 1990, 12, 973-986.***
50. ***Allmendinger, R.W.; Cardozo, N.; Fisher, D.M. Structural geology algorithms : Vectors and tensors. Cambridge New York Cambridge University Press: 2012.***
51. ***Vlaar, N.J.; van Keken, P.E.; van den Berg, A.P. Cooling of the earth in the archaean: Consequences of pressure-release melting in a hotter mantle. Earth and Planetary Science Letters 1994, 121, 1-18.***
52. ***Champion, D.C.; Smithies, R.H. Chapter 4.3 geochemistry of paleoarchean granites of the east pilbara terrane, pilbara craton, western australia: Implications for early archean crustal growth. In Developments in precambrian geology, van Kranendonk, M.J.; Smithies, R.H.; Bennett, V.C., Eds. Elsevier: 2007; Vol. 15, pp 369-409.***
53. ***Smithies, R.H.; Champion, D.C.; Van Kranendonk, M.J. Formation of paleoarchean continental crust through infracrustal melting of enriched basalt. Earth and Planetary Science Letters 2009, 281, 298-306.***
54. ***Van Kranendonk, M. Two types of archean continental crust: Plume <em>and</em> plate tectonics on early earth. American Journal of Science 2010, 310, 1187-1209.***
55. ***Jelsma, H.A.; Vinyu, M.L.; Wijbrans, J.R.; Verdurmen, E.A.T.; Valbracht, P.J.; Davies, G.R.; Valbracht, P.J. Constraints on archaean crustal evolution of the zimbabwe craton: A u-pb zircon, sm-nd and pb-pb whole-rock isotope study. Contributions to Mineralogy and Petrology 1996, 124, 55-70.***
56. ***Lin, S.; Beakhouse, G.P. Synchronous vertical and horizontal tectonism at late stages of archean cratonization and genesis of hemlo gold deposit, superior craton, ontario, canada. Geology 2013, 41, 359-362.***
57. ***Sanislav, I.V. Porphyroblast rotation and strain localization: Debate settled!: Comment. Geology 2010, 38, e204-e204.***
58. ***Dirks, P.H.G.M.; Jelsma, H.A.; Hofmann, A. Thrust-related accretion of an archaean greenstone belt in the midlands of zimbabwe. Journal of Structural Geology 2002, 24, 1707-1727.***
59. ***Cox, S.; Knackstedt, M.; Braun, J. Principles of structural control on permeability and fluid flow in hydrothermal systems. Reviews in Economic Geology 2001, 14, 1-24.***
60. ***Porter, C. Structural analysis and target generation, kukuluma-matandani area, geita greenstone belt, tanzania. Internal AngloGold Report, Geita Gold Mine 2002, 24.***
61. ***Schultz, R.A.; Fossen, H. Displacement–length scaling in three dimensions: The importance of aspect ratio and application to deformation bands. Journal of Structural Geology 2002, 24, 1389-1411.***

***62.*** ***Schultz, R.A.; Okubo, C.H.; Wilkins, S.J. Displacement-length scaling relations for faults on the terrestrial planets. Journal of Structural Geology 2006, 28, 2182-2193.***

***63.*** ***Ridley, J. The relations between mean rock stress and fluid flow in the crust: With reference to vein- and lode-style gold deposits. Ore Geology Reviews 1993, 8, 23-37.***

***64.*** ***Schultz, R.A.; Soliva, R.; Fossen, H.; Okubo, C.H.; Reeves, D.M. Dependence of displacement–length scaling relations for fractures and deformation bands on the volumetric changes across them. Journal of Structural Geology 2008, 30, 1405-1411.***

***65.*** ***Weinberg, R.F.; van der Borgh, P. Extension and gold mineralization in the archean kalgoorlie terrane, yilgarn craton. Precambrian Research 2008, 161, 77-88.***

***66.*** ***Dirks, P.H.G.M.; Charlesworth, E.G.; Munyai, M.R. Cratonic extension and archaean gold mineralisation in the sheba-fairview mine, barberton greenstone belt, south africa. South African Journal of Geology 2009, 112, 291-316.***

***67.*** ***Seward, T.M. The hydrothermal geochemistry of gold. In Gold metallogeny and exploration, Springer US: 1991; pp 37-62.***

***68.*** ***Seward, T.M. Thio complexes of gold and the transport of gold in hydrothermal ore solutions. Geochimica et Cosmochimica Acta 1973, 37, 379-399.***

***69.*** ***Kerrich, R.; Goldfarb, R.; Groves, D.; Garwin, S. The geodynamics of world-class gold deposits: Characteristics, space-time distribution, and origins. In Gold in 2000, Society of Economic Geologists, Inc.: 2000; Vol. 13, pp 501-551.***

***70.*** ***Campbell McCuaig, T.; Kerrich, R. P—t—t—deformation—fluid characteristics of lode gold deposits: Evidence from alteration systematics. Ore Geology Reviews 1998, 12, 381-453.***

***71.*** ***Likhoidov, G.G.; Plyusnina, L.P.; Shcheka, Z.A. The behavior of gold during listvenitization: Experimental and theoretical simulation. Doklady Earth Sciences 2007, 415, 723-726.***

***72.*** ***Chamberlain, C.M. Geology and genesis of the bulyanhulu gold deposit, sukumaland greenstone belt, tanzania. Unpublished PhD Thesis, Imperial College 2003, 410.***

***73.*** ***Chamberlain, C.M.; Tosdal, R.M. U–pb geochronology of the lake victoria greenstone terrane, tanzania. Mineral Deposit Research Unit, The University of British Columbia. Anglo-Gold Ashanti internal report 2007, 43.***

***74.*** ***Vos, I.M.A.; Bierlein, F.P.; Standing, J.S.; Davidson, G. The geology and mineralisation at the golden pride gold deposit, nzega greenstone belt, tanzania. Mineralium Deposita 2009, 44, 751.***

***75.*** ***Angelier, J.; Mechler, P. Sur une méthode graphique de recherche des contraintes principales également utilisable en tectonique et en séismologie: La méthode des dièdres droits. Bulletin de la Société Géologique de France 1977, 7, 1309-1318.***

***76.*** ***Delvaux, D.; Sperner, B. New aspects of tectonic stress inversion with reference to the tensor programme, in: Nieuwland, d.A. (ed.), new insights into structural***

***interpretation and modelling. . Geological Society of London, Special Publication 2003, 212, 75-100.***

***77. Angelier, J. Fault slip analysis and palaeostress reconstruction, in: Hancock, p.L. (ed.), continental deformation. Oxford, Pergamon, Oxford 1994, 101-120.***

***78. Etchecopar, A.; Vasseur, G.; Daignieres, M. An inverse problem in microtectonics for the determination of stress tensors from fault striation analysis. Journal of Structural Geology 1981, 3, 51-65.***

***79. Lisle, R.J. Principal stress orientations from faults: An additional constraint. Annales Tectonic 1987, 1, 155-158.***

***80. Allmendinger, R.W. Faultkinwin, version 1.1: A program for analyzing fault slip data for windows™. (www.Geo.Cornell.Edu/geology/faculty/rwa/programs.Html). 2001.***

***81. Cladouhos, T.T.; Allmendinger, R.W. Finite strain and rotation from fault slip data. Journal of Structural Geology 1993, 15, 771-784.***

***82. Molnar, P. Average regional strain due to slip on numerous faults of different orientations. Journal of Geophysical Research 1983, 88, 6430-6432.***

***83. Twiss, R.J.; Unruh, J.R. Analysis of fault slip inversions: Do they constrain stress or strain rate? Journal of Geophysical Research 1998, 101, 8335-8361.***

***84. Sperner, B.; Müller, B.; Heidbach, O.; D., D.; Reinecker, J.; Fuchs, K. Tectonic stress in the earth's crust: Advances in the world stress map project. In: Nieuwland, d.A. (ed.), new insights into structural interpretation and modelling. Geological Society of London Special Publication 2003, 212, 101-116.***

## 8. Appendix 1: Fault kinematic analysis

Kinematic data from faults can be used to reconstruct palaeo-stress fields [75]. To do this, information is required on the orientation of the fault plane, the slip direction visible as slickenlines, striations or gouge marks, and the sense of movement. Stress inversion techniques rely on the assumption that the slip direction coincides with the resolved shear stress on the fault plane, and that the set of faults used in the analysis, formed or were active in response to the same far field stress. Fault-slip data can be inverted to a reduced moment tensor with information on the direction of the principal stress axes and their relative size expressed as a stress ratio [76,77]. This reduced stress tensor can be calculated using the P (principal compression) and T (principal tension) axes that bisect the fault plane and an auxiliary plane perpendicular to the fault, by using least-square minimization techniques of direction cosines [49] or iterative methods that test a variety of possible tensor solutions [78]. Stress axes can also be determined graphically using the right dihedron method [76] [79], which constrains the orientation of principal stress axes by determining the area of maximum overlap of compressional and extensional quadrants for a suite of faults.

In analyzing the fault-slip data, we have used a linked Bingham distribution tensor calculated with the program FaultKinWin [80] following methods described by [49] and [81]. The FaultKinWin programme [80] uses the distribution of P and T axes for a suite of faults [75] to calculate a Bingham axial distribution based on a least squares minimization technique for direction cosines. In this technique the dihedral angle between the fault plane and an auxiliary plane is 90° and bisected by P and T axes. The eigenvectors for the calculated Bingham axial distribution provide average orientations for the maximum, minimum and intermediate concentration direction of the P and T axes, and the eigenvalues provide a measure of the relative concentration, or distribution of P and T axes. These eigenvalues vary between -0.5 and +0.5, with maximum values reached when P and T axes are perfectly concentrated. Variations in the eigenvalues (ev) can be linked to the stress regime using the relative size of the normalized eigenvalues expressed in a ratio, Rev, (with Rev = $[ev_2-ev_3]/[ev_1-ev_3]$) (constrictional stress: Rev = 1 with $ev_1 = ev_2$; plane stress: Rev = 0.5 with $ev_2 = 0$; flattening stress: Rev = 0 with $ev_2 = ev_3$). The FaultKinWin programme output is a plot of linked Bingham axes with eigenvalues and a related fault plane solution diagram displaying P and T quadrants in a manner similar to earthquake focal mechanisms (Figs 9, 10).

Although stress analysis from fault slip data is widely applied, debate continues whether the obtained solutions represent a stress field or provide a measure of strain and strain rate [82,83]. [49] and [80], using FaultKinWin, prefer to interpret the fault plane solutions as an indicator of strain rather than stress.

Here, the linked Bigham fault plane solution through FaultKinWin has been interpreted as an indication of the paleo-stress field. In doing this we are aware of the various pitfalls. Faults, once formed, can interact in complex ways in response to an imposed stress-field due to scale-dependent strain partitioning, complex fault interactions, block rotations, inhomogeneities in the rock mass etc. [83]. In spite of such limitations, the paleo-stress analysis technique has been successfully applied in a wide variety of tectonic settings [84] [20,66], and we believe it provides valuable insights in the tectonic controls on gold mineralization at Kukuluma and Matandani.

Misfits in collected datasets may have resulted from observational errors, the mixing of unrelated data points or limitations in the approach used. They can also be due to non-uniform stress fields as a result of fracture interactions, anisotropies in the rock mass, block rotations or slip partitioning. In near vertical shear fractures there is the added problem that a small rotation of the fracture plane around a horizontal axis can change it from a normal fracture compatible with the overall data set to a reverse fracture that is radically incompatible when using the computer programs. In calculating a Bingham tensor solution using FaultKinWin all data points were included. It is stressed that throughout the analyses of datasets, very few data points were incompatible with the final results, suggesting generally homogeneous data

As a general rule, the results from the paleo-stress analyses are best constrained for large data sets that combine fracture planes with different directions and movement sense. Thus, conjugate fracture sets, or Riedel, anti-Riedel and P-shear arrays provide good results more likely to be indicative of the regional paleo-stress field, especially if the stress inversion is based on at least 15 fracture planes [76,84], whilst sites in which only few planes, or planes in a limited number of directions can be measured provide at best an indication only of the local paleo-stress field, which may or may not conform with the regional results.